Simulation of precipitation/dissolution phenomena with large phase volume change using single-field C-CST model

C. Palka[a,b], S. Bordère[a,b], A. Lemoine[a,b], S. Glockner[a,b,*], A. Erriguible[a,b,c,*]

[a] Univ. Bordeaux, CNRS, Bordeaux INP, I2M, UMR 5295, F-33400, Talence, France
[b] Arts et Metiers Institute of Technology, CNRS, Bordeaux INP, I2M, UMR 5295, F-33400 Talence, France
[c] Univ. Bordeaux, CNRS, Bordeaux INP, ICMCB, UMR 5026, F-33600 Pessac, France

---

Abstract

This study presents a numerical approach for modelling diffusion-driven mass transfer in incompressible two-phase systems. We implemented the Compressive Continuous Species Transfer single-field formulation, utilising a Volume-of-Fluid approach with the CICSAM compressive scheme. While existing single-field methodologies successfully model dissolution phenomena, our investigation reveals that state-of-the-art discretisation approaches are inadequate for accurately modelling precipitation. Consequently, we introduced a shifted discretisation methodology, inspired by two-field formulation, for source terms involving mass transfer rate. This shifted method enables simulation of both dissolution and precipitation phenomena within the single-field framework. The approach is validated against analytical solutions across various dimensional scenarios, including novel theoretical solutions for 1D and 2D precipitation cases derived from existing 3D theoretical solutions. Finally, we demonstrate the method effectiveness by examining gas bubble mass transfer in creeping flow, comparing results with semi-analytical solutions and identifying limitations under high Péclet number conditions.

Keywords: Volume-of-fluid, Single-field formulation, Precipitation, Dissolution, Mass transfer, phase volume change, Multiphase flow.

---

[*] Corresponding author.

Email addresses: stephane.glockner@bordeaux-inp.fr (Stéphane Glockner), erriguible@enscbp.fr (Arnaud Erriguible)

Code availability: The implementation of the proposed method is made with `Notus` which significantly enhances the reproducibility of the present work. The original code is available in the Git repository https://git.notus-cfd.org/ (code v0.6.0).

1 Introduction

Mass transport and its transfer at interfaces in multiphase systems is a key aspect of numerous natural phenomena and industrial processes, ranging from geochemical reactions to chemical engineering applications, such as bubble column reactors, waste-water treatment facilities, chemical reactors and many others. These complex processes include viscous and capillary effects, chemical reactions and the coupling between mass transfer and fluid dynamics. This study focuses on modelling diffusion-driven mass transfer in an incompressible two-phase system consisting of a pure gas phase and a multicomponent liquid phase. Specifically, we examine systems where the gas species is diluted into the liquid phase referred to as the solution. Depending on whether the solution is undersaturated or supersaturated, the gas phase volume decreases or increases, generating dissolution or precipitation phenomena, respectively. As solute transport limits the kinetics, the interface is at thermodynamic equilibrium and is characterized by a concentration jump. Experimental measurements are generally expensive and limited by the available measuring techniques, which usually provide global quantities and do not give information about local details, such as local mass transfer rates. Numerical simulation is therefore a powerful tool to investigate these processes.

Studies in the literature initially addressed the numerical modelling of mass transfer without accounting for phase volume change through various methodologies. These approaches are based on conventional multiphase flow techniques such as: (*i*) the Level Set (LS) method (Sussman et al. (1994)), employed in subsequent studies (Yang and Mao (2005); Deshpande and Zimmerman (2006); Wang et al. (2008); Hayashi et al. (2014); Balcázar-Arciniega et al. (2019); Yu and Leung (2025)); (*ii*) the Front Tracking (FT) approach (Tryggvason et al. (2001)), used in (Khinast et al. (2003); Radl et al. (2008); Aboulhasanzadeh et al. (2012)); and (*iii*) the Volume-of-Fluid (VOF) approach (Hirt and Nichols (1981); Scardovelli and Zaleski (1999)), implemented in (Haroun et al. (2010); Marschall et al. (2012); Deising et al. (2016); Maes and Soulaine (2018); Farsoiya et al. (2021); Tourbier et al. (2024)). Additional methodologies include Arbitrary Lagrangian-Eulerian (ALE) methods (Bäumler (2014); Lehrenfeld (2015); Weber et al. (2017)) and hybrid VOF-LS methods (Taqieddin et al. (2020); Schulz et al. (2022)), amongst other significant contributions to the field.

In comparison, few studies in the literature have addressed the numerical modelling of mass transfer while accounting for phase volume change. The complexity arises from two major challenges: first to account for phase volume variations induced by mass transfer while maintaining the concentration discontinuity at interfaces, and second, to deal with the mass volume changes that occur when species transfer between liquid and gas phases. In diffusion-driven mass transfer problems, the analysis of phase volume change induced by the mass transferred between two phases has been performed using the VOF methods through two approaches: the single-field (or one-fluid) approach (Maes and Soulaine (2020); Vachaparambil and Einarsrud (2020); Zanutto et al. (2022b); Zanutto et al. (2022a)) and the two-field (or two-fluid) approach (Fleckenstein and Bothe (2015); Gennari et al. (2022)). These two VOF methods differ in their conceptualization. Rather than solving separate species transport equations in each phase and then closing the system through interface conditions, as employed in two-field approaches, the single-field formulation utilises a unified methodology. This approach incorporates the principles of species flux conservation, both in the bulk phases and at the interface, into one comprehensive set of equations. This approach is referred to in the literature as the Continuous Species Transfer (CST) model (Haroun et al. (2010); Deising et al. (2016)) and, more recently, the Compressive Continuous Species Transfer (C-CST) model (Maes and Soulaine (2018); Maes and Soulaine (2020)).

In this work, the C-CST single-field formulation will be implemented in the `Notus` open-source CFD software Notus (2024) using a VOF approach based on the Compressive Interface Capturing Scheme for Arbitrary Meshes (CICSAM) of Ubbink and Issa (1999) for both volume fraction and species transport equations. This scheme allows sharp interface representation by effectively preventing interface smearing. The objective is to remove the use of an artificial numerical compressive term typically used within the C-CST single-field framework (Zanutto et al. (2022b)) with diffusive advection scheme such as Flux Corrected Transport (FCT) scheme of Zalesak (1979).

Fleckenstein and Bothe (2015) proposed a one-fluid formulation of the Navier–Stokes equations along with the transport equation for the phase indicator function. This formulation, which assumes incompressible and Newtonian fluids, serves as the foundation for both single-field and two-field approaches. Fleckenstein's study reported highly accurate dissolution results that showed excellent agreement with both analytical predictions and experimental observations.

Building upon this foundation, Maes and Soulaine (2020) replaced the two-field formulation formulation of the species conservation equation by the equation derived by Haroun et al. (2010) and Deising et al. (2016). This formulation assumes that all species are diluted within the solvent. Maes also derived an expression for the mass transfer rate term that accounts for phase volume variation within the single-field framework, representing the first demonstration of pure gas dissolution into a liquid by using this formulation. More recently, Zanutto et al. (2022b) enhanced this approach by eliminating the need for additional numerical treatments, employing instead a compressive advection scheme for both the species conservation equation and the transport of the phase indicator function. However, this development was exclusively applied to dissolution cases. Therefore, among the studies addressing mass transfer phenomena with phase volume change, it is noteworthy that every study examines dissolution processes, whereas the precipitation problem remains largely unexplored in the literature. While the two-field formulation has recently demonstrated accurate predictions of precipitation phenomena (Gennari et al. (2022)), comparable results have not yet been achieved within the single-field framework.

However, we will show that state-of-the-art numerical modelling of single field C-CST method fails to reproduce precipitation phenomena. To address this issue, we propose to use a two-field numerical methodology developed by Gennari et al. (2022) for diffusion-driven problems and build upon the work of Palmore and Desjardins (2019); Scapin et al. (2020); Malan et al. (2021) (in temperature-driven problems). This original discretisation of mass transfer rate aims to improve the computational capabilities of the single-field C-CST model to match those of the two-field formulation in diffusion-driven mass transfer problems for both dissolution and precipitation phenomena.

The implementation of the C-CST model will first be validated against the theoretical solution of Crank (1979) for a 1D-dissolution case and the approximate solution of Epstein and Plesset (1950) for a 3D-dissolution case. Additionally, it will be tested against the theoretical solution of Scriven (1959) for a 3D-precipitation case. To address a crucial gap in the literature, this paper aims to make a contribution by developing novel 1D and 2D theoretical solutions for static precipitation phenomena, building upon the work of Scriven (1959). This comprehensive approach enables our study to compare the C-CST discretisation methodology commonly used in the literature with the discretisation methodology inspired from the two-field formulation, across a variety of static dissolution and precipitation scenarios.

This work is organised as follows. The governing equations are presented in Section 2. The single-field formulation leading to the C-CST model is described in Section 3. The details of the numerical implementation of the C-CST model and methodology for the discretisation of mass transfer rates, inspired from two field formulation are given in Section 4. Subsequently, the implementation of the model is validated by comparison with analytical solutions: in 1D and 3D for dissolution phenomena in Section 5, and in 1D, 2D and 3D for precipitation phenomena in Section 6, where the exact solutions for all dimensions are provided. Finally, the methodology is applied to study mass transfer of gas bubbles in creeping flow. The results are compared with a semi-analytical solution for dissolving bubbles in creeping flow, and a precipitation case is presented to demonstrate the efficiency of the proposed method in dynamic scenarios in Section 7.

2 Governing equations

In this section, we describe the continuum mechanical modelling of momentum and mass transfer in incompressible multi-phase flow with volume effects. For this purpose, we consider a physical generic domain Ω composed of two separate phases, the liquid phase Ω^l and the gas phases Ω^g as we are interested in gas/liquid mass transfer. These two phases are separated by the interface Σ as shown in the Fig. 1, where $\boldsymbol{n_\Sigma}$ represents the normal vector directed from the liquid phase toward the gas phase. Note that the subscript l and g refer to the liquid and gas phases, respectively.

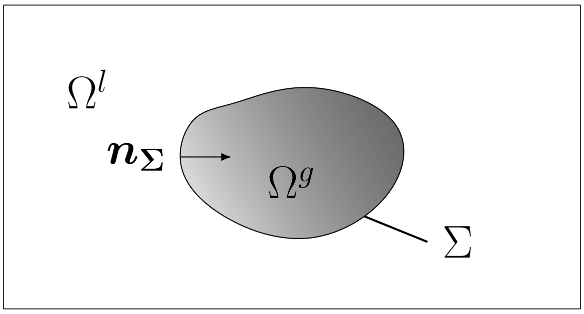

Figure 1 – Schematic representation of the considered physical domain $\Omega = \Omega^l \cup \Omega^g$.

In any multicomponent mass transfer system, each phase k consist of a mixture of n chemical components. In this system, every component i is characterized locally by its partial density

$\rho_{i,k} = \rho_{i,k}(\boldsymbol{x}, t)$, where $i \in [\![1, \ldots, n]\!]$. This partial density is a function that varies with both spatial coordinates $\boldsymbol{x}$ and time t. Under conditions where no chemical reaction occurs, the mass conservation principle for each component is described by:

$$\frac{\partial \rho_{i,k}}{\partial t} + \nabla \cdot (\rho_{i,k} \boldsymbol{u_{i,k}}) = 0 \quad \text{in} \quad \Omega^k \backslash \Sigma, \quad k = g, \, l, \tag{1}$$

where $\boldsymbol{u_{i,k}}$ represents the velocity of component i in phase k. By definition, the total density of phase k is defined as the sum of individual component partial densities: $\rho_k = \sum_i \rho_{i,k}$. Similarly, the barycentric velocity of phase k is expressed as $\rho_k \boldsymbol{u_k} = \sum_i \rho_{i,k} \boldsymbol{u_{i,k}}$. By applying these definitions and summing (Eq. 1) over all n component, we obtain the mass conservation equation for phase k given by:

$$\frac{\partial \rho_k}{\partial t} + \nabla \cdot (\boldsymbol{u_k} \rho_k) = 0 \quad \text{in} \quad \Omega^k \backslash \Sigma, \quad k = g, \, l. \tag{2}$$

Assuming incompressible phases with constant properties, we can derive the simplified form (Eq. 3) of the mass conservation equation

$$\nabla \cdot \boldsymbol{u_k} = 0 \quad \text{in} \quad \Omega^k \backslash \Sigma, \quad k = g, \, l. \tag{3}$$

Additionally, the momentum conservation equation for the bulk of each phase k (valid for incompressible and Newtonian fluids), is expressed as:

$$\frac{\partial \rho \boldsymbol{u_k}}{\partial t} + \nabla \cdot (\rho_k \boldsymbol{u_k} \otimes \boldsymbol{u_k}) = -\boldsymbol{\nabla} p_k + \boldsymbol{\nabla} \cdot (2\mu_k \boldsymbol{S_k}) + \rho_k \boldsymbol{g} \quad \text{in} \quad \Omega^k \backslash \Sigma, \quad k = g, \, l, \tag{4}$$

where $\boldsymbol{g}$ denotes the gravitational body force applied to the system, and $\boldsymbol{S_k} = \frac{1}{2}\left(\nabla \boldsymbol{u_k} + \nabla^{\mathsf{T}} \boldsymbol{u_k}\right)$ represents the strain-rate tensor. The terms p_k and μ_k correspond to the pressure and dynamic viscosity of phase k, respectively.

By rearranging the mass conservation equation (Eq. 1), the species conservation equations (Eq. 5) are obtained. These advection-diffusion equations are expressed as

$$\frac{\partial \rho_{i,k}}{\partial t} + \nabla \cdot (\boldsymbol{F_{i,k}}) + \nabla \cdot (\boldsymbol{J_{i,k}}) = 0 \quad \text{in } \Omega^k / \Sigma, \quad k = g, \, l, \tag{5}$$

where $\boldsymbol{F_{i,k}} = \rho_{i,k}\boldsymbol{u_k}$ denotes the advective mass flux and $\boldsymbol{J_{i,k}}$ represents the mass diffusion flux of species i in phase k, which is expressed through Fick's law Taylor and Krishna (1993) as $\boldsymbol{J_{i,k}} = -D_{i,k}\boldsymbol{\nabla}\rho_{i,k}$, where $D_{i,k}$ denotes the diffusion coefficient of species i in phase k. The diffusive flux of component n can be obtained with

$$\boldsymbol{J_{n,k}} = -\sum_{1\leq i<n} \boldsymbol{J_{i,k}}, \tag{6}$$

resulting in $n-1$ equations to solve.

To establish a complete system of equations, the continuity of conservative quantities are required at the interface Σ for each equation. To describe the discontinuity of quantities across the interface Σ, we introduce the jump notation for any quantity Γ, denoted by $[\![\Gamma]\!]$, which is defined as

$$[\![\Gamma]\!](\boldsymbol{x}) = \lim_{h\to 0^+} \left(\Gamma(\boldsymbol{x}+h\boldsymbol{n_\Sigma}) - \Gamma(\boldsymbol{x}-h\boldsymbol{n_\Sigma})\right). \tag{7}$$

Using this notation, the mass conservation principle at the interface (closing (Eq. 3)) is given by:

$$[\![\rho_k\left(\boldsymbol{u_k}-\boldsymbol{u_\Sigma}\right)]\!]\cdot\boldsymbol{n_\Sigma} = 0 \quad \text{on } \Sigma, \tag{8}$$

where $\boldsymbol{u_\Sigma}$ denotes the interface velocity. Finally, the term inside the bracket

$$\dot{m}_k := \rho_k\left(\boldsymbol{u_k}-\boldsymbol{u_\Sigma}\right)\cdot\boldsymbol{n_\Sigma} \quad \text{on } \Sigma,$$

represents the mass flux of phase k at the interface Σ.

The momentum conservation principle at the interface (closing Eq. 4) is expressed as:

$$[\![p_k\boldsymbol{I} - 2\mu_k\boldsymbol{S_k}]\!]\cdot\boldsymbol{n_\Sigma} = \sigma\kappa\boldsymbol{n_\Sigma} \quad \text{on } \Sigma, \tag{9}$$

where $\boldsymbol{I}$ denotes the unit tensor, σ the interfacial tension coefficient, and κ the interface mean curvature.

The mass flux conservation principle at the interface (closing (Eq. 5)) is expressed as:

$$[\![(\rho_{i,k}\left(\boldsymbol{u_k} - \boldsymbol{u_\Sigma}\right) - D_{i,k}\boldsymbol{\nabla}\rho_{i,k}) \cdot \boldsymbol{n_\Sigma}]\!] = 0 \quad \text{on } \Sigma, \tag{10}$$

where the term inside the brackets

$$\dot{m}_{i,k} := \left(\rho_{i,k}\left(\boldsymbol{u_k} - \boldsymbol{u_\Sigma}\right) - D_{i,k}\boldsymbol{\nabla}\rho_{i,k}\right) \cdot \boldsymbol{n_\Sigma} \quad \text{on } \Sigma,$$

represents the mass flux of component i in phase k.

Finally, thermodynamic equilibrium imposes the equality of chemical potentials at the interface through Henry's law Henry and Banks (1803), which relates the species concentration on either side of the interface as

$$\rho_{i,l} = H_i \rho_{i,g} \quad \text{on } \Sigma, \tag{11}$$

where H_i is the Henry's coefficient for species i.

3 Single-field C-CST model

In this study, the single-field formulation is used. More detailed information can be found in Slattery (1999). This VOF method expresses the conservation equations for mass, momentum, and species—initially defined separately for each phase—into a unified system of equations valid across the entire numerical domain Ω. This formulation, based on the Conditional Volume Averaging (CVA) techniques, applies the volume averaging operator to a generic variable Γ in a control volume V as

$$\overline{\Gamma} = \frac{1}{|V|}\int_V \Gamma dV. \tag{12}$$

In this context, the variables are expressed using global (or mixture) variables defined as:

$$\Gamma = \alpha_g \overline{\Gamma}^g + \alpha_l \overline{\Gamma}^l, \tag{13}$$

where α_g and α_l are the phase indicator function of the gas and liquid phase respectively. The mean phasic notation $\overline{\Gamma}^k$ appears and defined as

$$\overline{\Gamma}^{k} = \frac{1}{|V_k|} \int_{V_k} \Gamma dV. \tag{14}$$

Global variables, defined across the entire domain independently of the phase occupying the cells (gas, liquid, or mixture), include phase properties such as density ρ, dynamic viscosity μ, pressure p and transported variables such as velocity $\boldsymbol{u}$ and partial species densities ρ_i.

The single-field system of equations is presented below. This system is the same as the one used in the literature by Maes and Soulaine (2020) and Zanutto et al. (2022b). More details can be found in these papers, as well as in Fleckenstein and Bothe (2015) for the derivation of the Navier-Stokes equation. Only the final conservation laws are presented.

3.1 Species conservation equations: C-CST model

The single-field species conservation equation called C-CST (Compressive Continuous Species Transfer), derived by Maes and Soulaine (2018) from (Eq. 5) and (Eq. 10), is expressed as

$$\frac{\partial \rho_i}{\partial t} + \nabla \cdot (\rho_i \boldsymbol{u}) + \nabla \cdot \left(\frac{(1 - H_i)\, \rho_i}{\alpha_g + H_i\,(1 - \alpha_g)} \alpha_g \alpha_l \boldsymbol{u_r} \right) = \nabla \cdot \left(D_i^{SF} \boldsymbol{\nabla} \rho_i + \boldsymbol{\phi_i} \right), \tag{15}$$

where $\boldsymbol{u}$ represents the velocity obtained from Navier-Stokes equations, $\boldsymbol{u_r} = \overline{\boldsymbol{u_g}}^{g} - \overline{\boldsymbol{u_l}}^{l}$ denotes the relative velocity, the additional diffusion term $\boldsymbol{\phi_i}$ represents the CST (Continuous Species Transfer) flux and D_i^{SF} (Single-Field diffusion coefficient) denotes the equilibrium-based mean diffusion coefficient derived by Maes and Soulaine (2020) and expressed as

$$D_i^{SF} = \frac{\alpha_g \overline{D_{i,g}}^{g} + H_i\,(1 - \alpha_g)\, \overline{D_{i,l}}^{l}}{\alpha_g + H_i\,(1 - \alpha_g)}. \tag{16}$$

This expression for the equilibrium-based mean diffusion coefficient indicates that in cells containing an interface, the diffusion coefficient is weighted by the Henry's coefficient H_i. The terms $\overline{D_{i,g}}^{g}$ and $\overline{D_{i,l}}^{l}$ represent the phase-averaged diffusion coefficients in the gas and liquid phases, respectively. When these values are not space-dependent, they are equivalent to the phase diffusion coefficients $D_{i,g}$ and $D_{i,l}$. This notation is used in the following sections since these diffusion coefficients are constant.

Finally, the additional diffusion term $\boldsymbol{\phi_i}$ (Eq. 17), called CST flux was introduced by Haroun et al. (2010). It accounts for the discontinuous variation of concentration at the interface and it is expressed as

$$\boldsymbol{\phi_i} = \rho_i \frac{1 - H_i}{\alpha_g + (1 - \alpha_g) H_i} D_i^{SF} \boldsymbol{\nabla} \alpha_g. \tag{17}$$

The C-CST model is a more accurate form of (Eq. 5) than the CST model used by Haroun et al. (2010) and formally derived by Deising et al. (2016) where additional assumptions were made. Indeed, the CST model simplifies the expression of the advective fluxes $\boldsymbol{F_i}$ as

$$\boldsymbol{F_i} = \alpha_g \overline{\rho_{i,g} \boldsymbol{u_g}}^g + \alpha_l \overline{\rho_{i,l} \boldsymbol{u_l}}^l = \rho_i \boldsymbol{u} + \left(\overline{\rho_{i,g}}^g - \overline{\rho_{i,l}}^l \right) \alpha_g (1 - \alpha_g) \boldsymbol{u_r} \approx \rho_i \boldsymbol{u}. \tag{18}$$

This simplification is justified because the relative velocity $\boldsymbol{u_r}$ is negligible compared to the velocity intensity obtained from the Navier-Stokes equations $\boldsymbol{u}$ as shown by Fleckenstein and Bothe (2015), even for systems with high solubilities (such as CO_2 in H_2O).

However, within the single-field framework and the use of a diffusive advection scheme (Flux Corrected Transport (FCT) method called Multidimensional Universal Limiter with Explicit Solution (MULES) Weller (2008)), a compressive velocity $\boldsymbol{u}_{\text{comp}}$ is used to reduce diffusion of the scheme specially in advection dominant flow (Maes and Soulaine (2020)). This compressive velocity $\boldsymbol{u}_{\text{comp}}$ is expressed as (Rusche (2002)):

$$\boldsymbol{u}_{\text{comp}} = \left[\min \left(c_\alpha \frac{|F_f|}{A_f}, \max_f \left(\frac{F_f}{A_f} \right) \right) \right] \boldsymbol{n_\Sigma}, \tag{19}$$

where c_α is a compression constant whose value (generally between 0 and 4) depends on the user settings. F_f represents the volumetric flux across the face f and A_f is the surface of these face. It replaces the relative velocity $\boldsymbol{u_r}$ in equations (Eq. 15) and (Eq. 26).

Note that the magnitude of $\boldsymbol{u}_{\text{comp}}$ (Eq. 19) is known to be much higher than that of the relative velocity. This distinction in the naming of the variable is made to clarify the role of the term: $\boldsymbol{u_r}$ is a physical velocity whereas $\boldsymbol{u}_{\text{comp}}$ is a "numerical" one in order to reduce diffusion of the interface. Zanutto et al. (2022b) showed that the use of the CICSAM (Compressive Interface Capturing Scheme for Arbitrary Meshes) scheme, developed by Ubbink and Issa (1999), with its compressive properties and high resolution capabilities, eliminates the need of the terms containing $\boldsymbol{u}_{\text{comp}}$.

3.2 Navier-Stokes and phase advection equation

The single-field formulation of the continuity equation, (Eq. 3) and (Eq. 8), leads to a non-zero divergence at the interface, which represents the variation in mass volume between the phases. This equation reads

$$\nabla \cdot \boldsymbol{u} = -\dot{m}\left(\frac{1}{\rho_g} - \frac{1}{\rho_l}\right), \tag{20}$$

where ρ_g, ρ_l denote the densities of the gas and liquid phase respectively. The right-hand side of this equation is obtained by using the mass flux conservation principle at the interface (Eq. 8) and $\dot{m}$ describes the rate of mass transferred between the two phases across their interface. Since this work focuses on gas-liquid mass transfer, it is important to note that the total volume interfacial mass transfer rate, $\dot{m}$, represents the cumulative contribution of each volume species mass transfer rate $\dot{m}_i$ that occurs at the interface Σ:

$$\dot{m} = \sum_{1 \leq i \leq n} \dot{m}_i, \tag{21}$$

where the volume species mass transfer rate $\dot{m}_i$ is defined as the sum over the phase of the integral of the partial mass flux of component i crossing the interface Σ in a reference volume V. Its expression is given by:

$$\dot{m}_i = \sum_k \alpha_k \frac{1}{V} \int_\Sigma \dot{m}_{i,k} dS. \tag{22}$$

This interfacial mass transfer rate $\dot{m}$ occurs only at the interface Σ between the liquid and gas phases and accounts for the phases volume change when the thermodynamic equilibrium of the overall system is not reached. It is expressed from (Eq. 21) and (Eq. 22) by Maes and Soulaine (2020) as

$$\dot{m} = \frac{\sum_i \left(D_i^{SF} \boldsymbol{\nabla} \rho_i - \boldsymbol{\phi_i}\right)}{1-\alpha_g} \cdot \boldsymbol{\nabla} \alpha_g. \tag{23}$$

This expression for $\dot{m}$ clearly demonstrates the coupling between the species conservation equation and the Navier-Stokes equations.

Further, the single-field momentum equation of (Eq. 4) and (Eq. 9) can be written as

$$\frac{\partial \rho \boldsymbol{u}}{\partial t} + \boldsymbol{\nabla} \cdot (\rho \boldsymbol{u} \otimes \boldsymbol{u}) = -\boldsymbol{\nabla} p + \boldsymbol{\nabla} \cdot (2\mu \bar{\bar{\epsilon}}) + \rho \boldsymbol{g} + \boldsymbol{f_\Sigma}. \tag{24}$$

The surface tension force, denoted as $\boldsymbol{f_\Sigma}$, acts as a body force at the interface following the continuum surface force modelled by Brackbill et al. (1992) as

$$\boldsymbol{f_\Sigma} = \sigma \kappa \boldsymbol{\nabla} \alpha_g, \tag{25}$$

where σ denotes the surface tension coefficient and κ the mean curvature.

The phase indicator function advection equation is then given by:

$$\frac{\partial \alpha_g}{\partial t} + \nabla \cdot (\alpha_g \boldsymbol{u}) + \nabla \cdot (\alpha_g \alpha_l \boldsymbol{u_r}) = -\frac{\dot{m}}{\rho_g}. \tag{26}$$

This equation is exact and requires no additional assumptions (Graveleau et al. (2017)). The right-hand side term derives directly from the interfacial mass conservation principle (Eq. 8). The left-hand side terms containing $\boldsymbol{u_r}$ are non-zero only at the interface and can be neglected as previously discussed in section 3.1. This equation is the same as the one derived by Badillo (2012). Moreover, under the assumption of incompressible phases, they demonstrate that the advective flux due to the relative velocity can be expressed as:

$$\nabla \cdot (\alpha_g \alpha_l \boldsymbol{u_r}) = (1 - 2\alpha_g) \nabla \cdot \boldsymbol{u} \tag{27}$$

This formulation allows the expression of this term in any dimension without the need to interpolate the velocity across the interface.

Finally, the single-field C-CST model consists of four partial differential equations: (Eq. 15), (Eq. 20), (Eq. 24) and (Eq. 26) representing species, mass and momentum conservation and phase advection, respectively.

4 Numerical methods

The C-CST model described above has been implemented in `Notus` (Notus (2024)), our in-house Fortran-based CFD code. This parallel computational framework solves the system of equations formed by (Eq. 15), (Eq. 20), (Eq. 24) and (Eq. 26) using finite volume methods on a fixed Cartesian staggered grid. In this context (unless explicitly stated otherwise), scalar variables are defined and computed at the cell centres of the mesh, while vector components are defined and computed at the cell faces. An Euler implicit time discretisation is used with a second-order centered scheme for the diffusion in the momentum and species conservation equations, except for the term involving $\boldsymbol{\phi_i}$, whose discretisation will be described below. The coupling between velocity and pressure fields in the incompressible Navier-Stokes equations ((Eq. 20) and (Eq. 24)) is solved using the incremental pressure correction method developed by Goda (1979). The source term in the mass conservation equation (Eq. 20) is incorporated into the incremental pressure correction step.

An algebraic VOF method is used to solve the phase indicator transport equation (Eq. 26). Following Perrier et al. (2019) and Zanutto et al. (2022b), we implemented the implicit CICSAM method, that uses a switching techniques between two formulations: the Hyper-C scheme (Leonard (1991)) and the ULTIMATE-QUICKEST scheme (Ubbink and Issa (1999)), for the compressive differencing scheme (CDS) and high-resolution scheme (HR) respectively. This switching mechanism depends on both the interface orientation and its movement. More details about its implementation can be found in Ubbink and Issa (1999). This scheme is used to advect both the phase indicator transport and the species conservation equations, ensuring consistency between these equations (Deising et al. (2016)). This choice eliminates the terms involving $\boldsymbol{u}_{\text{comp}}$, as the interface remains sharp.

Finally, the mean curvature κ, in the continuum surface force (Eq. 25), is determined using the height function method (Popinet (2009)).

4.1 Numerical discretisation of the CST flux

One of the key challenges in this modelling approach lies in the discretisation of the C-CST model (Eq. 15). The discretisation methodology used in this work follows the approaches developed by Zanutto et al. (2022b) and Maes and Soulaine (2020). In the diffusion term, the face value mean equilibrium-based diffusion coefficient $D_{i,f}^{SF}$ is evaluated as

$$D_{i,f}^{SF} = \frac{\alpha_{g,f} D_{i,g} + H_{i,f} \left(1 - \alpha_{g,f}\right) D_{i,l}}{\alpha_{g,f} + H_{i,f} \left(1 - \alpha_{g,f}\right)}. \tag{28}$$

Here $\alpha_{g,f}$ and $H_{i,f}$ represent the volume fraction of the gas phase and Henry's coefficient, respectively, evaluated at the centre of the face f through a linear interpolation from cell values.

For the integration of the CST flux $\nabla \cdot \boldsymbol{\phi_i}$, the term $\boldsymbol{\phi_i}$ is reformulated as

$$\boldsymbol{\phi_i} = D_i^{SF} \beta_i \rho_i \boldsymbol{\nabla} \alpha_g, \tag{29}$$

where β_i is a scalar expressed as

$$\beta_i = \frac{1 - H_i}{\alpha_g + H_i \left(1 - \alpha_g\right)}. \tag{30}$$

The term β_i requires particular attention, as highlighted by Zanutto et al. (2022b). As the diffusion term is treated in an implicit way, $\beta_i \rho_i$ are evaluated at the face centre using a linear interpolation. More details can be found in Zanutto et al. (2022b).

4.2 Interfacial mass transfer rate discretisation

4.2.1 The literature unshifted method

The mass transfer rate $\dot{m}$ occurs exclusively at the interface between the liquid and gas phases. This term accounts for both phase density change in (Eq. 20) and phase volume evolution in (Eq. 26). Maes and Soulaine (2020) established the mathematical formulation of $\dot{m}$ (Eq. 23) for implementation within the single-field framework. This expression takes into account the additional diffusion flux $\boldsymbol{\phi_i}$ resulting from the discontinuous variation of species partial density across the interface. Regarding its discretisation, Zanutto et al. (2022b) highlighted its importance. Following the work of Maes and Soulaine (2020), they reformulated the expression of $\dot{m}$ into two separate terms. Using the definition of the following vector $\boldsymbol{\Phi_D}$

$$\boldsymbol{\Phi_D} = \frac{\sum_i \left(D_i^{SF} \boldsymbol{\nabla} \rho_i - \boldsymbol{\phi_i}\right)}{1 - \alpha_g}, \tag{31}$$

the expression of $\dot{m}$ becomes:

$$\dot{m} = \boldsymbol{\Phi_D} \cdot \boldsymbol{\nabla} \alpha_g = \nabla \cdot \left(\boldsymbol{\Phi_D} \alpha_g\right) - \alpha_g \nabla \cdot \left(\boldsymbol{\Phi_D}\right). \tag{32}$$

This reformulation allows the discretisation of $\boldsymbol{\Phi_D} \alpha_g$ to be performed using upwinding in the direction of $\boldsymbol{\nabla}\alpha_g$, which prevents negative values in the transport of the phase indicator function (Eq. 26). Without such a discretisation, Zanutto et al. (2022b) showed that the simulations would not produce usable results. For the second term, $\nabla \cdot (\boldsymbol{\Phi_D})$ is expressed as

$$\nabla \cdot (\boldsymbol{\Phi_D}) = \nabla \cdot \left(\frac{\sum_i \left(D_i^{SF} \boldsymbol{\nabla} \rho_i - D_i^{SF} \Psi_i \boldsymbol{\nabla} \alpha_g \right)}{1 - \alpha_g} \right), \tag{33}$$

with

$$\Psi_i = \rho_i \frac{1 - H_i}{\alpha_g + H_i \left(1 - \alpha_g\right)}.$$

The discretisation is naturally performed by computing all scalar quantities in (Eq. 33) at the centre of the cells, followed by linear interpolation to the face centres. This discretisation of $\dot{m}$ is used in this study due to its demonstrated stability in the work of Zanutto et al. (2022b). More details of this integration can be found in Zanutto et al. (2022b), where this discretisation is referred to as 'model 1'.

This method is called the "unshifted method" as the source terms containing $\dot{m}$ are discretised on the interface where $0 < \alpha_g < 1$ since it takes non-zero values only in these cells. It has demonstrated its effectiveness for dissolution problems in both one-dimensional static systems and three-dimensional dynamic scenarios involving dissolving rising bubbles. As we will show in section 6, this method fails in the modelling of precipitation phenomena. To overcome these difficulties, we propose the shifted method described in the following section 4.2.2.

4.2.2 The shifted method inspired from two-field formulation

Inspired by the work of Gennari et al. (2022) within the two-field framework, we propose to shift the computation of $\dot{m}$ within the gas phase. Also known as the velocity extension algorithm, this shifted method was developed and successfully implemented by Gennari et al. (2022). Originally introduced by Hardt and Wondra (2008), the algorithm was designed to reduce numerical instabilities arising when the source term is distributed across a narrow layer of cells, which may not yield a divergence-free velocity field in all liquid and mixed cells. Gennari et al. (2022) adopted this approach to ensure a divergence-free velocity in the liquid phase with minimal computational effort, in contrast to the method employed by Hardt and Wondra (2008), which requires solving an additional Helmholtz equation.

The first implementation step involves computing the rate of mass transfer $\dot{m}$ (using (Eq. 32) and the model 1 proposed by Zanutto et al. (2022b)) within interfacial cells. The interfacial cells, where the value of $\dot{m}$ is different from zero, are designated as donor cells. For every donor cell with coordinates (i, j), a centred stencil of size $(2n + 1) \times (2n + 1)$, where n denotes the stencil size, is defined on the donor cell. Within this stencil, every cell presenting a volume fraction $\alpha_g = 1$ is designated as an acceptor cell. The number of these acceptor cells per donor cells is stored in the field avg as illustrated in Fig. 2a. Note that if there is zero acceptor cell within the stencil, we increase its size n. A donor (acceptor) may have multiple acceptors (donors).

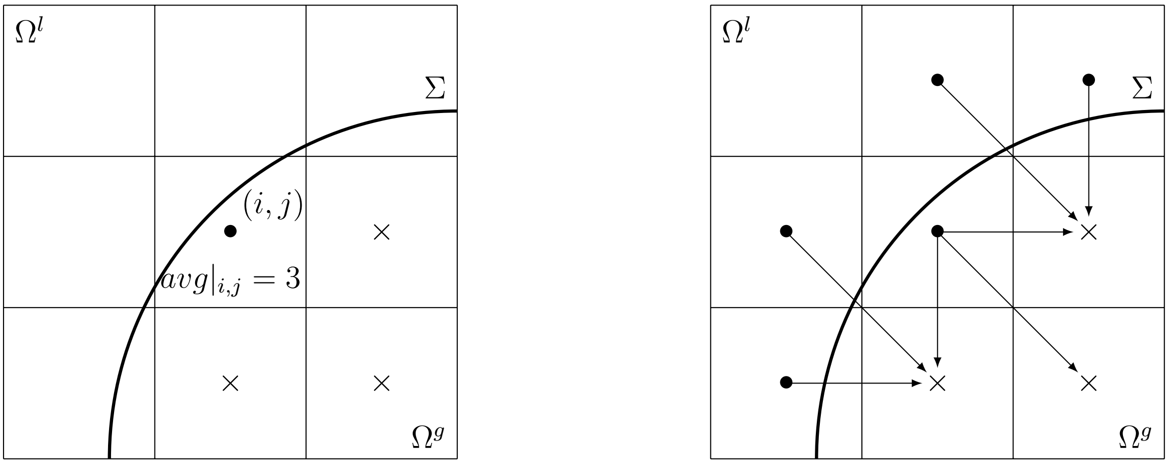

(a) (b)

Figure 2 – 2D illustration of the steps involved in calculating mass transfer rate $\dot{m}'$. The acceptor cells are marked with the symbol ×, and the reference donor cell is marked with the symbol •, (a) calculation of the field $avg|_{i,j}$ related to cell indexed (i, j). Here $avg|_{i,j} = 3$ and the stencil size is 1 ; (b) example of computation of $\dot{m}'$. The contribution is equal to $\frac{\dot{m}}{avg}$.

The second step is the redistribution of the mass transfer rate term $\dot{m}$. For each acceptor, the contribution from all its relative donors is computed and stored in the new field $\dot{m}'$, which is defined only for acceptor cells and set to null for the others, as illustrated in (Fig. 2b). This displacement of the source term ensures that the total mass transferred between phases per unit of time is conserved. Finally, the rate of mass transfer $\dot{m}$ is replaced in (Eq. 20) (in the projection step of the Navier-Stokes equations) and in (Eq. 26), respectively as

$$\nabla \cdot \boldsymbol{u} = -\dot{m}' \left(\frac{1}{\rho_g} - \frac{1}{\rho_l} \right), \tag{34}$$

and

$$\frac{\partial \alpha_g}{\partial t} + \nabla \cdot (\alpha_g \boldsymbol{u}) = -\frac{\dot{m}'}{\rho_g}. \tag{35}$$

The shifted method relocates the source term initially computed at the interface in a narrow layer of cells close to Σ in the gas phase. The acceptor cells receive information from their respective donor cells, regardless of the mass transfer direction (*i.e.* from liquid to gas or vice versa). Consequently, the new field $\dot{m}'$ remains zero in the liquid phase and at the interface.

5 Dissolution Validation

In this section, the proposed method is validated through several test cases used in the literature for dissolution phenomena. The aim is to validate the shifted method with dissolution problems used in the literature. In this section and the following, we recall that, the gas phase is a pure phase only constituted by A-component while the liquid phase is a dilute solution of A-component into B-component. Only the diffusion of the A-component is studied. Both cases studied in this section are static cases in which the phases are not subjected to flow or volume forces such as gravity.

5.1 1D-validation of dissolution phenomena

The 1D-dissolution serves as a fundamental model for analysing phase change phenomena. The model describes a planar interface separating liquid and gas phases, where the dissolution of the gas phase into the liquid medium generates fluid flow and interface movement. This benchmark case aims to validate critical aspects: *(i)* the interfacial mass transfer calculation, *(ii)* the volume variation of the gas phase and *(iii)* the accurate capture of the discontinuous variation of concentration at the interface. The analysis examines the diffusion of a single chemical species, denoted as A. The saturation ratio ζ_i of a generic species i is defined to compare the initial concentration in the liquid phase $\rho_{i,l}^0$ to the thermodynamic equilibrium density $\rho_{i,l}^*$ of the liquid phase imposed by Henry's law (Eq. 11). This saturation ratio is expressed as

$$\zeta_i = \frac{\rho_{i,l}^0}{\rho_{i,l}^*}. \tag{36}$$

In agreement with these notations, $\rho_{i,g}^{0}$ denotes the initial concentration and $\rho_{i,g}^{*}$ the thermodynamic equilibrium density of species i in the gas phase. In the initial state, the liquid phase is characterized by a saturation ratio $\zeta_A = 0$ ($i.e.$ $\rho_{A,l}^{0} = 0$), while the gas phase consists purely of species A (where $\rho_{A,g}^{0} = \rho_{A,g}^{*} = \rho_g$).

Table 1 – Properties of the gas and liquid phases.

Phase	Density $[\mathrm{kg\,m^{-3}}]$	Viscosity $[\mathrm{N\,s\,m^{-2}}]$
liquid	1×10^{3}	1.05×10^{-3}
gas	1	1.46×10^{-5}

For this class of problems, Crank (1979) derived an exact solution that provides both the concentration profile (Eq. 37) and the kinetics of phase volume change (Eq. 38)

$$\rho_{A,l}\left(x,t\right) = H_A \rho_g \left(1 - \operatorname{erf}\left(\frac{x - l_i}{2\sqrt{D_{A,l} t}}\right)\right), \tag{37}$$

$$l_I(t) = 2 H_A \rho_g \sqrt{\frac{D_{A,l} t}{\pi}}. \tag{38}$$

The system properties are detailed in Table 1, with analyses conducted for two diffusion coefficients: $D_{A,l} = 1 \times 10^{-6}\,\mathrm{m^2\,s^{-1}}$ and $D_{A,l} = 1 \times 10^{-8}\,\mathrm{m^2\,s^{-1}}$. By defining the Schmidt number Sc to compare the diffusion of momentum to the diffusion of mass, as

$$\mathrm{Sc} = \frac{\mu_l}{\rho_l D_{A,l}}. \tag{39}$$

These diffusion coefficients correspond to Schmidt numbers of $\mathrm{Sc} = 1.05$ and $\mathrm{Sc} = 1.05 \times 10^{2}$, respectively. Both cases employ a Henry's coefficient $H_A = 5 \times 10^{-1}$.

The simulation domain extends to a length of $L = 10 L_{\mathrm{ref}}$, where the characteristic length L_{ref} equals $1 \times 10^{-2}\,\mathrm{m}$. Initially, the interface is positioned at $l_I(t = 0) = 0$, with the gas phase occupying the left region $(-L/2 \le x \le l_I)$ and the liquid phase occupying the right region $(l_I \le x \le L/2) : x/L_{\mathrm{ref}} \in [\![-5, 5]\!]$. The boundary conditions of the species conservation equation (Eq. 15) and Navier-Stokes equations (Eq. 20), (Eq. 24) include a Neumann condition at $x = L$ and symmetry conditions at all other domain boundaries. The computational mesh consists of 1600 uniform cells along the x-axis. The simulation is performed using a time step $\delta t = 1 \times 10^{-4}\,\mathrm{s}$. The reference time is $t_{\mathrm{ref}} = \frac{\rho_l L_{\mathrm{ref}}^2}{\mu_l}$, and the reference concentration equals the gas phase concentration, where $\rho_{A,\text{ref}} = \rho^*_{A,g} = 1$.

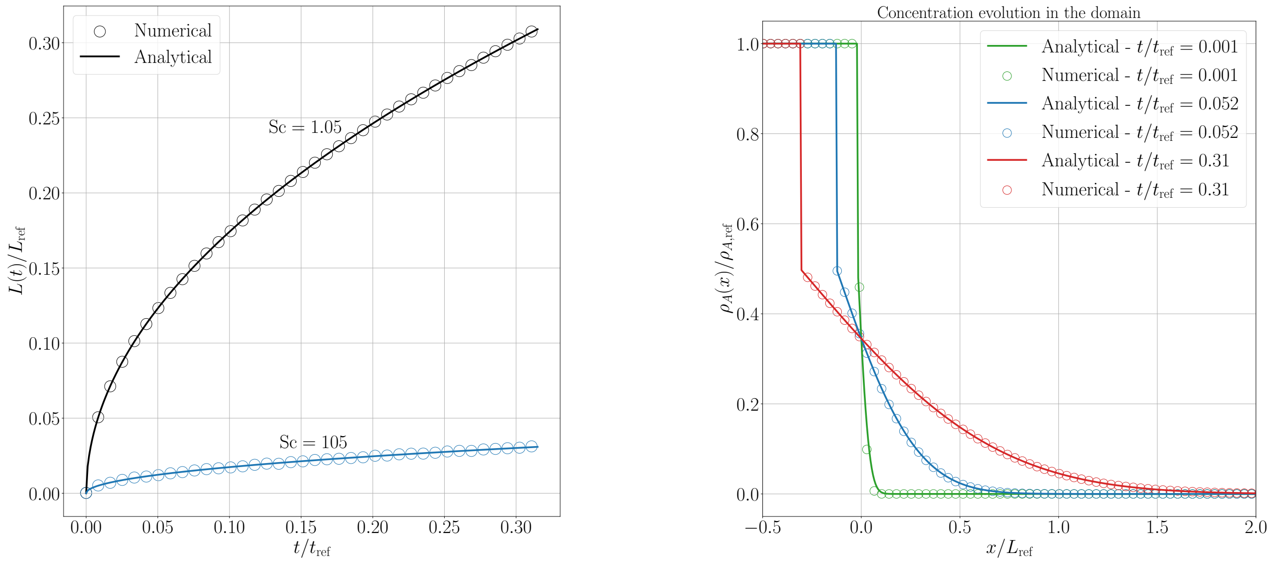

(a) (b)

Figure 3 – Validation results of the 1D-dissolution problem for a Henry's coefficient $H_A = 5\times10^{-1}$ and a saturation ratio $\zeta_A = 0$. As both unshifted and shifted methods led identical results, only the results of the unshifted method are presented. (a) Interface kinetics for two Schmidt numbers : $\text{Sc} = 1.05$ and $\text{Sc} = 1.05 \times 10^2$ and (b) concentration profile along the x-axis at different simulation times for the case $\text{Sc} = 1.05$.

Fig. 3 shows the results obtained with both unshifted and shifted methods proposed in this work. Since the results for both methods are strictly superposed, only the results of the unshifted method are presented and called "Numerical". Fig. 3a presents the numerical results for interface kinetics in both cases, compared against the theoretical solution (Eq. 38). The simulations accurately predict the interface position $l_I(t)$ in agreement with theory for both Schmidt numbers. Fig. 3b displays the concentration profiles for the more diffusive case $\text{Sc} = 1.05$. Comparison with theoretical concentration profiles (Eq. 37) demonstrates that the model effectively captures the concentration discontinuity at the interface over time, while accounting for the gas phase volume variation.

5.2 3D-validation of dissolving bubble in an undersaturated solution

To finalize the dissolution validation process, a study of dissolving bubble is performed. In 3D, an analytical solution exists for a similar problem in which the advective mass flux relative to the mass transfer (Eq. 20) is neglected. This solution was established by Epstein and Plesset (1950) for a domain where the inner boundary is a sphere of constant radius R:

$$\begin{aligned}
&\frac{\partial \rho_A}{\partial t} = \nabla \cdot \left(D_{A,c} \boldsymbol{\nabla} \rho_A \right), \\
&\rho_A \left(r, t=0 \right) = \rho^0_{A,l} && \text{for } r > R, \\
&\rho_A \left(R, t \right) = \rho^*_{A,l} && \text{for } t > 0, \\
&\lim_{r \to \infty} \rho_A \left(r, t \right) = \rho^0_{A,l} && \text{for } t > 0.
\end{aligned} \tag{40}$$

The solution to equation (Eq. 40) can be used to approximate the case of a bubble exchanging matter with the surrounding liquid phase ($i.e.$ where R is time dependant). According to Duda and Vrentas (1971), this quasi-steady approximation is accurate as long as mass transfer is slow ($i.e.$ the effects of liquid velocity are negligible compared to diffusion) and the growth of the concentration boundary layer is rapid compared to the dissolution rate. The solution, expressed in terms of the radius of the sphere, is

$$\dot{R} = \frac{D_A \left(\rho^0_{A,l} - \rho^*_{A,l} \right)}{\rho_g} \left[\frac{1}{R} + \frac{1}{\sqrt{\pi D_{A,l} t}} \right]. \tag{41}$$

When the full system of equations is solved numerically, including mass flux relative to the mass transfer (Eq. 20), the radius evolution R predicted by the Epstein-Plesset (EP) model (Eq. 41) overestimates the experimental shrinkage velocity by approximately 10% in an air-water system (Duncan and Needham (2004)). To account for this discrepancy, a correction factor is applied to the theoretical solution, resulting in what will be referred to as the corrected EP model.

The computational domain consists of a cube with sides of length $30L_{\text{ref}}$. A composite mesh strategy was implemented, which comprises two regions: a uniform mesh within a central cube of length $l_u = 4L_{\text{ref}}$ with 50 cells per diameter, and a non-uniform (exponential variation of step size) mesh in the remaining domain. The liquid phase has an initial concentration of A $\rho^0_{A,l} = 0$ giving a saturation ratio $\zeta_A = 0$. The properties of the phases are indexed in Table 1 and a Henry's coefficient $H_A = 2 \times 10^{-1}$ is used with a diffusion coefficient $D_{A,l} = 2 \times 10^{-5}\,\mathrm{m^2\,s^{-1}}$, corresponding to a Schmidt number of $\mathrm{Sc} = 5.25 \times 10^{-2}$. The simulation is performed using a time step $\delta t = 1 \times 10^{-4}\,\mathrm{s}$. Only one eighth of the sphere is simulated by applying symmetry condition on the corresponding boundaries. The other boundary conditions include a Neumann condition for the species conservation equation (Eq. 15) and Navier-Stokes equations (Eq. 20), (Eq. 24).

The results on the evolutions of the radius over time are shown in Fig. 4. As both methods produced identical results, only the unshifted method's results are displayed, labelled as 'Numerical'. As described by Duncan and Needham (2004), there is a discrepancy between the full model simulation and the solution provided by the EP model of Epstein and Plesset (1950). Nevertheless, taking into account the experimental observations mentioned earlier, we observe that the simulation results align with the corrected prediction of the EP model. The slight deviation is of the same order as the one observed in the two-field methodology (Gennari et al. (2022)).

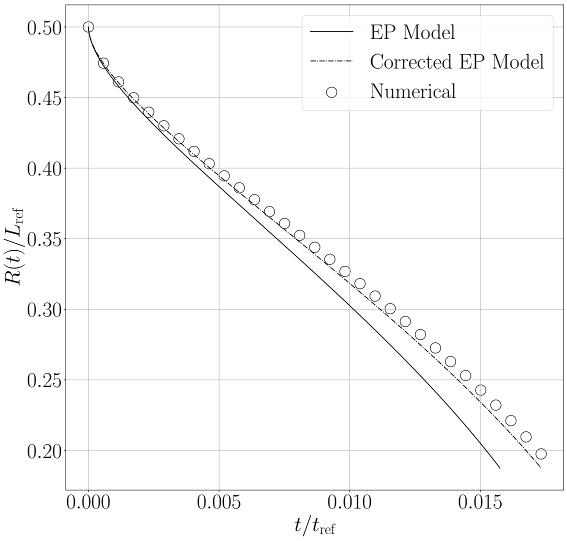

Figure 4 – Temporal evolution of the bubble radius and comparison with the EP model, with and without correction of 10%. It corresponds to a Henry's coefficient $H_A = 2 \times 10^{-1}$, a saturation ratio of $\zeta_A = 0$ and a Schmidt number of $\text{Sc} = 5.25 \times 10^{-2}$. As both unshifted and shifted methods led identical results, only the results of the unshifted method are presented.

6 Theoretical solutions and validation for precipitation phenomena

In this section, we use the 3D precipitation static test case of Scriven (1959) and propose two additional 1D and 2D analytical solutions of the same problem. This approach addresses a significant gap in the existing literature, which previously only provided a theoretical solution for the three-dimensional scenario. By extending the theoretical framework to 1D and 2D cases, we enable a comprehensive comparative analysis between the unshifted and shifted methods across all dimensional representations of precipitation problems.

6.1 Analytical solutions for 1D, 2D and 3D cases

In this section, we examine a system consisting of a pure gas phase immersed in a supersaturated solution ($\zeta_A > 1$), with chemical species A being the unique component of the gas phase. The analysis excludes volume forces, ensuring the centre of mass remains stationary. The phase properties remain consistent with previous specifications, as detailed in Table 1. Our investigation proceeds systematically through dimensionally progressive test cases.

The exact solution for this type of problems was originally developed by Scriven (1959) for a spherical geometry (3D), yielding an equation that describes the time evolution of the sphere radius R as

$$R(t) = 2\kappa_{\varepsilon,\tau}\sqrt{D_{A,l}t}, \tag{42}$$

where the dimensionless factor $\kappa_{\varepsilon,\tau}$ depends on several key parameters: the densities of the gas (ρ_g) and liquid (ρ_l) phases, the concentration of species A in the liquid phase at $r \to \infty$ ($\rho^{\infty}_{A,l}$), and the interfacial concentration determined by Henry's law ($\rho^{*}_{A,l}$). This factor is determined by solving for $\kappa_{\varepsilon,\tau}$ the following equation

$$-1 = 2\tau\kappa^3_{\varepsilon,\tau}\exp\left(\kappa^2_{\varepsilon,\tau} + 2\varepsilon\kappa^2_{\varepsilon,\tau}\right)\int_{\kappa_{\varepsilon,\tau}}^{\infty}\eta^{-2}\exp\left(-2\varepsilon\kappa^3_{\varepsilon,\tau}\eta^{-1} - \eta^2\right)\,\mathrm{d}\eta, \tag{43}$$

where $\eta = \dfrac{1}{2}\dfrac{r}{\sqrt{D_{A,l}t}}$ and r is the radius corresponding to the spatial variation. Constants τ and ε are expressed as

$$\tau = \frac{\rho_g}{\rho_l}\frac{\rho_l - \rho^*_{A,l}}{\rho^*_{A,l} - \rho^\infty_{A,l}} \quad \text{and} \quad \varepsilon = \frac{\rho_l - \rho_g}{\rho_l}. \tag{44}$$

In the literature, several articles attempt to extend this equation to 2D configurations, such as Vachaparambil and Einarsrud (2020). These extended solutions rely on the computation of correlations for the dimensionless factor $\kappa_{\varepsilon,\tau}$. Wang et al. (2016) successfully used a 3D correlation for $\kappa_{\varepsilon,\tau}$ that provides a good approximation of (Eq. 43). Nevertheless, these correlations are not mathematically exact and are less accurate, especially in 2D. Here, we derived an exact 1D and 2D solutions for the factor $\kappa_{\varepsilon,\tau}$, which varies as a function of the configuration dimension n. For more details on the derivation of these solutions, refer to section 8. We present here only the final form of these theoretical solutions.

As a function of the configuration dimension n ($n = 1$ for 1D, $n = 2$ for 2D, and $n = 3$ for 3D), the factor $\kappa_{\varepsilon,\tau}$ is the solution of (Eq. 45)

$$-1 = \frac{2\tau\kappa_{\varepsilon,\tau}}{F(\kappa_{\varepsilon,\tau})}\int_{\kappa_{\varepsilon,\tau}}^{\infty} F(\eta)\,\mathrm{d}\eta, \tag{45}$$

where we introduce the function $F(\eta)$ expressed as

$$F(\eta) = \begin{cases} \exp(2\varepsilon\kappa_{\varepsilon,\tau}\eta - \eta^2) & \text{if } n = 1, \\ \eta^{-1}\exp\left(2\varepsilon\kappa^2_{\varepsilon,\tau}\ln(\eta) - \eta^2\right) & \text{if } n = 2, \\ \eta^{-2}\exp\left(-2\varepsilon\kappa^2_{\varepsilon,\tau}\eta^{-1} - \eta^2\right) & \text{if } n = 3. \end{cases} \tag{46}$$

From this solution, we can also derive the associated concentration profile of the solute $\rho_A(r,t)$:

$$\rho_A(r,t) = \frac{2\tau\kappa_{\varepsilon,\tau}}{F(\kappa_{\varepsilon,\tau})}\int_{\kappa_{\varepsilon,\tau}}^{\eta} F(\eta)d\eta. \tag{47}$$

We have thus established the exact solutions for both kinetics (Eq. 45) and evolving concentration profiles (Eq. 47) for all dimensional representations. Note that when $\rho_l = \rho_g$ the derived equations returns the solution given by Zener (1949).

6.2 1D-validation of precipitation phenomena

In this case, the domain has the same characteristics as the one used in the 1D-validation of dissolution phenomena in section 5.1. The domain length varies from $10L_{\text{ref}}$ to $20L_{\text{ref}}$ in function of the interface kinetics. The mesh number varies from 1600 to 3200 in order to maintain cell dimensions while maintaining their uniformity. As in the previous test case, initially, the interface is positioned at $l_I(t = 0) = R_0 = 0$, with the gas phase occupying the left region ($-L/2 \leq x \leq l_I$) and the liquid phase occupying the right region ($l_I \leq x \leq L/2$). The liquid phase has an initial concentration $\rho^0_{A,l}$ and a Henry's coefficient $H_A = 2 \times 10^{-1}$ is used. The initial concentration of species A in the solution is $\rho^0_{A,l}$ corresponding to $\zeta_A > 1$ since different cases are studied. In every case, the simulation is performed using a time step $\delta t = 1 \times 10^{-4}\,\text{s}$.

On the first hand, a diffusion coefficient $D_{A,l} = 2 \times 10^{-5}\,\text{m}^2\,\text{s}^{-1}$ is used, corresponding to $\text{Sc} = 5.25 \times 10^{-2}$. The reference parameters are the same as the one defined in section 5.1. In Fig. 5, the numerical results obtained with the unshifted method are presented while those obtained with the new shifted discretisation of source terms are shown in Fig. 6. The results are compared across three different kinetic cases against the theoretical solution (Eq. 42), where $\kappa_{\varepsilon,\tau}$ was computed using $n = 1$ and $\rho^{\infty}_{A,l} = \rho^0_{A,l}$, since the concentration at the boundaries remains constant. These three cases are defined based on the value of the saturation ratio ζ_A, ranging from 2 to 4, in order to simulate a broad range of kinetics behaviours. For both methods, evolving concentration profiles was plotted for the faster interface displacement and compared to the theoretical solutions given by (Eq. 47). A resume of tested cases can be found in Table 2 referred to as case 1, 2 and 3.

As shown in Fig. 5a, the unshifted method cannot accurately predict the interface position $R(t)$. The results indicate that the predicted kinetics are faster than the theoretical ones. Mainly due to the poor captures of the concentration profiles within the liquid phase as shown in Fig. 5b even if an accurate concentration jump is obtained.

However, Fig. 6a shows that the shifted method allow to accurately predict the interface position $R(t)$ in agreement with theoretical expectations. Fig. 6b displays the evolving concentration profiles and demonstrates that the model effectively captures the concentration discontinuity at the interface over time, while accounting for the gas phase volume variation.

On the other hand, to further challenge the shifted method presented in this study, more

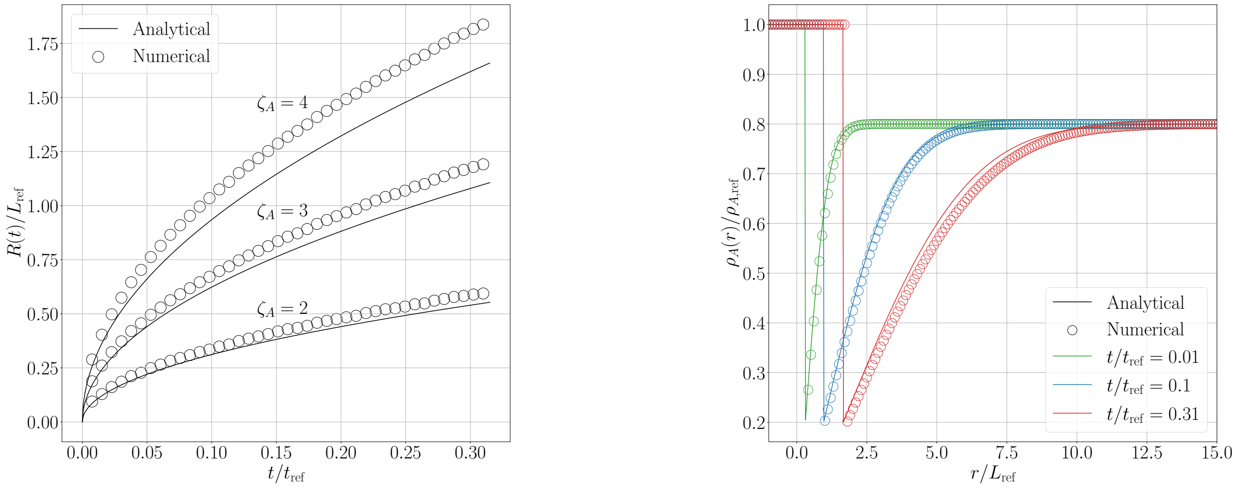

(a) (b)

Figure 5 – Numerical results for a 1D precipitation case by using the unshifted method. They correspond to a Henry's coefficient $H_A = 2 \times 10^{-1}$. (a) Interface kinetics for three different supersaturation $\zeta_A \in [\![2, 4]\!]$ and (b) concentration profiles along the x-axis for a saturation ratio $\zeta_A = 4$.

Table 2 – Summary of tests cases conducted in the context of 1D-precipitation. The dimensionless factor $\kappa^{1D}_{\varepsilon,\tau}$ is determined from the analytical solution (Eq. 45) for $n = 1$.

Case	ζ_A	H_A	τ	$\kappa^{1D}_{\varepsilon,\tau}$	Sc
case 1	2	2×10^{-1}	-5	0.1129	5.25×10^{-2}
case 2	3	2×10^{-1}	-2.5	0.2258	5.25×10^{-2}
case 3	4	2×10^{-1}	-1.66	0.3387	5.25×10^{-2}
case 4	9	1×10^{-1}	-1.25	0.4516	5.25×10^{-2}
case 5	90	1×10^{-2}	-1.12	0.5024	5.25×10^{-2}
case 6	90	1×10^{-2}	-1.12	0.5024	5.25

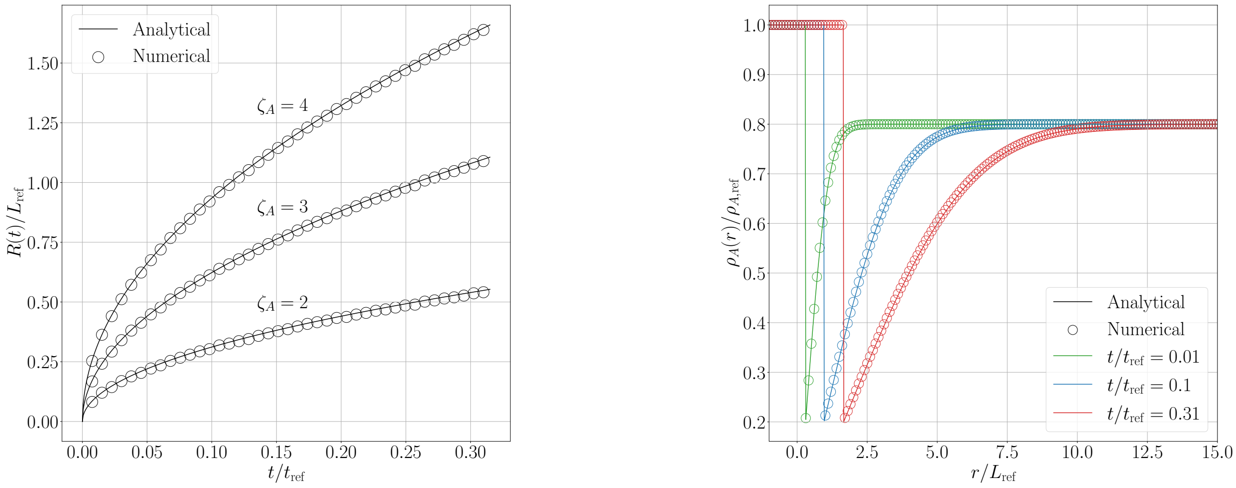

(a) (b)

Figure 6 – Numerical results for a 1D precipitation case by using the shifted method presented in this study. They correspond to a Henry's coefficient $H_A = 2 \times 10^{-1}$. (a) Interface kinetics for three different supersaturation $\zeta_A \in [\![2, 4]\!]$ and (b) concentration profiles along the x-axis for a saturation ratio $\zeta_A = 4$.

complex configurations are tested. Three of them, listed in Table 2, are presented in this article in Fig. 7 in order to simulate an even broad range of kinetics behaviours. First, the initial concentration $\rho^0_{A,l}$ is increased to achieve $\zeta_A = 9$, while using a Henry's coefficient $H_A = 1 \times 10^{-1}$. In the next case, the Henry's coefficient is reduced by a factor of 10. This reduction enables the simulation of a significant species concentration discontinuity at the interface, characterized by $\zeta_A = 90$ and $H_A = 1 \times 10^{-2}$. In the final case, the kinetics is slowed by using a diffusion coefficient $D_{A,l} = 2 \times 10^{-7}\,\mathrm{m}^2\,\mathrm{s}^{-1}$, corresponding to a Schmidt number of $\mathrm{Sc} = 5.25$. Finally as shown in Fig. 7a, the simulation accurately predicts the interface position $R(t)$ in agreement with theoretical expectations for the three configurations tested as well as the concentration profiles plotted for the slowest case in Fig. 7b that demonstrate that the model effectively captures the concentration discontinuity at the interface over time, even while accounting for huge discontinuous concentration variation.

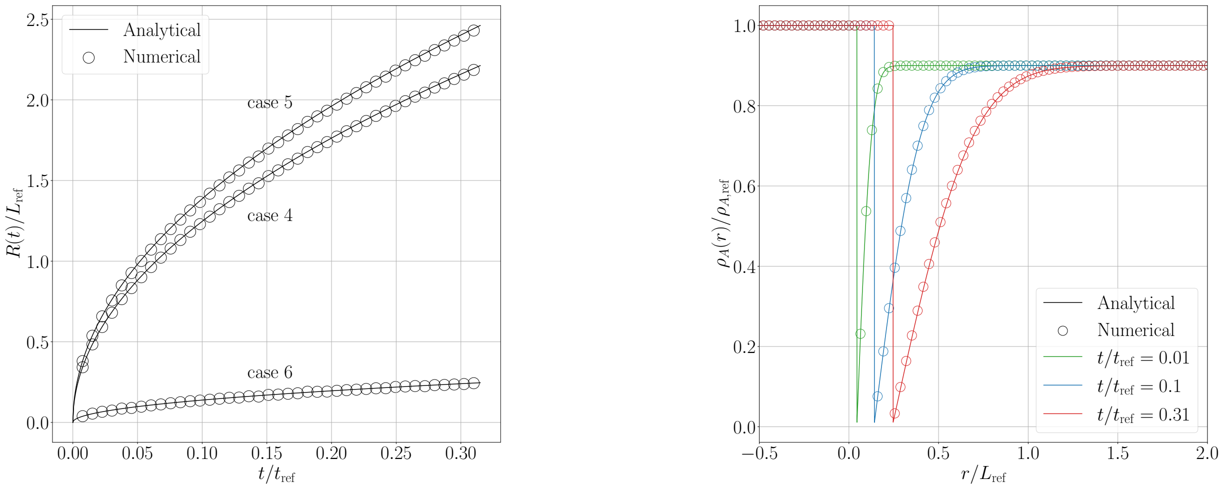

(a) (b)

Figure 7 – Numerical results for three other 1D precipitation cases by using the shifted method presented in this study. In these cases, both Henry's coefficient H_A and saturation ratio ζ_A vary. (a) Interface kinetics for three different supersaturations listed in Table 2 and referred to as case 4, 5, 6 and (b) concentration profiles for the slower case (*i.e.* case 6) along the x-axis.

6.3 2D, 3D-validation of precipitation phenomena

Simulations were also performed on a circle (2D) and a sphere (3D) immersed in a supersaturated solution ($\zeta_A > 1$). In both cases, the computational domain consists of a square (cube in 3D) with sides of length $30L_{\mathrm{ref}}$. A composite mesh strategy was implemented, which comprises two regions: a uniform mesh within a central square (cube in 3D) of length l_u ranging from $4L_{\mathrm{ref}}$ to $10L_{\mathrm{ref}}$ (depending on the kinetics) with 50 cells per diameter, and a non-uniform (exponential variation of step size) mesh in the remaining domain. The initial configuration consists of a gas phase with a diameter of $D_b = L_{\mathrm{ref}} = 1 \times 10^{-2}\,\mathrm{m}$, while the liquid phase, characterized by an initial concentration of $\rho^0_{A,l}$, occupies the remainder of the domain. The properties of the phases are reported by Table 1. The system employs Neumann boundary conditions and a Henry's coefficient $H_A = 2 \times 10^{-1}$ is used. The theoretical solutions for the radius and concentration profile are provided by (Eq. 42) and (Eq. 47), respectively, as function of time. In these solutions, $\kappa_{\varepsilon,\tau}$ was computed using (Eq. 45) with $n = 2$ for the 2D case (respectively $n = 3$ for the 3D case) and $\rho^\infty_{A,l} = \rho^0_{A,l}$, since the concentration at the boundaries remains constant. Finally, a diffusion coefficient of $D_{A,l} = 2 \times 10^{-5}\,\mathrm{m}^2\,\mathrm{s}^{-1}$, corresponding to a Schmidt number of $\mathrm{Sc} = 5.25 \times 10^{-2}$, was selected to accelerate mass transfer and reduce computational resources while allowing observation of significant phase volume changes within reasonable simulation times ($\dot{m} \propto D_{A,l}$). A summary of the simulated test cases is provided in Table 3 where simulations was performed using a time step $\delta t = 1 \times 10^{-4}\,\mathrm{s}$.

In both cases, the concentration field is initialized by using the theoretical profile (Eq. 47) to follow the methodology employed by Gennari et al. (2022). Indeed, while equation (Eq. 42) indicates that the gas phase is initially non-existent at $t = 0\ s$ (i.e., $R(t = 0) = 0$), the Volume of Fluid (VOF) approach requires an initialization of the volume fraction α_g. This necessitates generating the gas phase with an initial radius $R(t_0) = R_0$. Here, t_0 represents the time required to reach R_0, which can be determined using

$$t_0 = \frac{1}{D_A} \frac{R_0^2}{4\kappa_{\varepsilon,\tau}^2}. \tag{48}$$

These initial conditions ensure a concentration field around the circle (and the sphere) that is consistent with their initial sizes. To optimize computational resources, the 3D simulation was conducted on one-eighth of the sphere using symmetry conditions. For the 2D simulations, three domain configurations were tested: a complete domain model, a half-domain model, and a quarter-domain model. Symmetry conditions were applied in both the half and quarter configurations. The results obtained from all three configurations demonstrated complete consistency, validating the symmetry-based approach used in the 3D configurations.

Table 3 – Summary of tests cases conducted in the context of 2D/3D-precipitation with the shifted method developed in this paper. The dimensionless factor $\kappa_{\varepsilon,\tau}^{2D}$ and $\kappa_{\varepsilon,\tau}^{3D}$ are determined from the analytical solution (Eq. 45) for $n = 2$ and $n = 3$, respectively.

ζ_A	H_A	τ	$\kappa_{\varepsilon,\tau}^{\mathrm{2D}}$	$\kappa_{\varepsilon,\tau}^{\mathrm{3D}}$	Sc
2	2×10^{-1}	-5	0.2876	0.4205	5.25×10^{-2}
3	2×10^{-1}	-2.5	0.4802	0.6687	5.25×10^{-2}
4	2×10^{-1}	-1.66	0.6589	0.8942	5.25×10^{-2}

Contrary to the exploitable results obtained with the unshifted method in 1D-precipitation, this method did not give satisfactory results for these specific cases. Indeed, in the simulation carried out with this method, the interface was highly unstable and distorted circle and sphere interface.

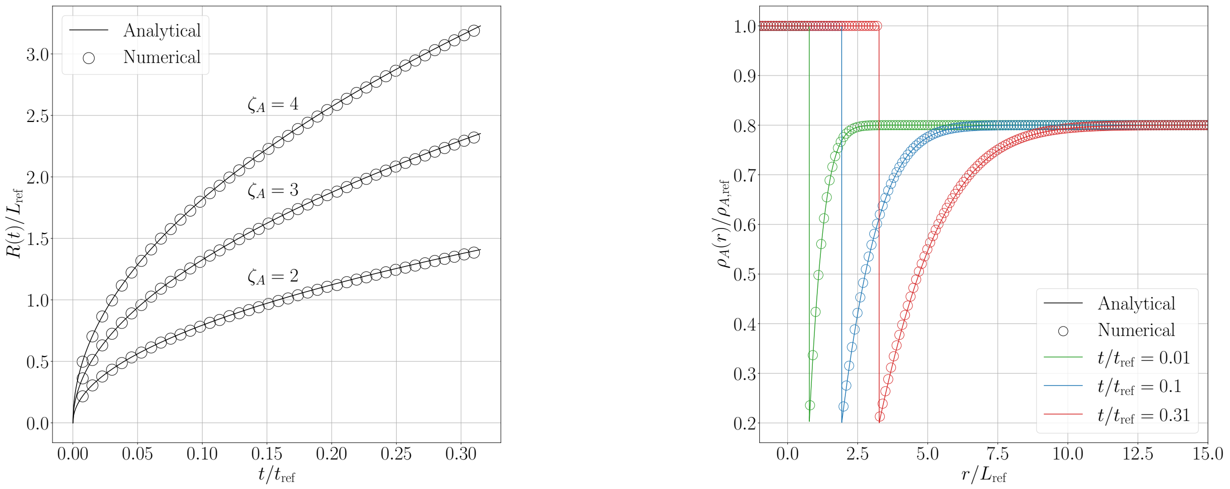

(a) (b)

Figure 8 – Numerical results for a 2D precipitation case by using the shifted method presented in this study. They correspond to a Henry's coefficient $H_A = 2 \times 10^{-1}$. (a) Interface kinetics for three different saturation ratios $\zeta_A \in [\![2, 4]\!]$ listed in Table 3 and (b) concentration profiles along the r-axis for a saturation ratio $\zeta_A = 4$.

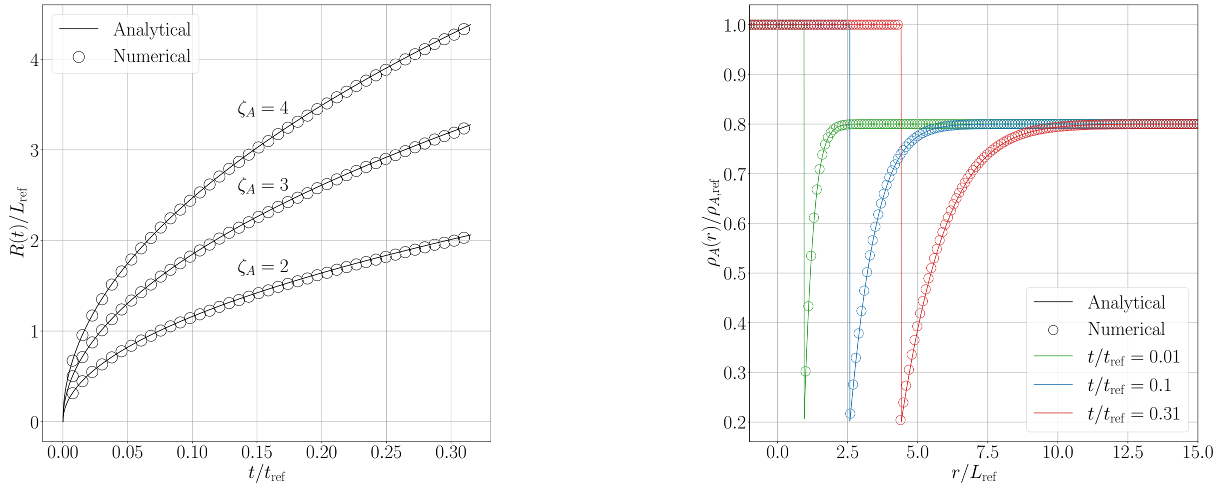

(a) (b)

Figure 9 – Numerical results for a 3D precipitation case by using the shifted method presented in this study. They correspond to a Henry's coefficient $H_A = 2 \times 10^{-1}$. (a) Interface kinetics for three different saturation ratios $\zeta_A \in [\![2, 4]\!]$ listed in Table 3 and (b) concentration profiles along the r-axis for a saturation ratio $\zeta_A = 4$.

Therefore, the shifted method proposed in this paper was used to obtain the results shown in Fig. 8 and Fig. 9 for the 2D and 3D simulations, respectively. The temporal evolution of the circle and sphere radii, compared against theoretical solutions, is presented in Fig. 8a and Fig. 9a. Furthermore, Fig. 8b and Fig. 9b display the concentration profiles for the case $\zeta_A = 4$, alongside their corresponding theoretical solutions. The numerical results demonstrate excellent agreement with theoretical solutions across all tested supersaturation values. The proposed shifted method successfully captures both the interface and concentration discontinuities with high accuracy in both spatial dimensions.

7 Mass transfer from a gas bubble in creeping flow with phase volume change

7.1 Dissolution

Every test cases presented so far were made in static conditions in which the phases were not subjected to flow or volume forces such as gravity. To our best of knowledge, there is a unique test case to validate the implementation of the model for a moving bubble exchanging matter with the surrounding undersaturated liquid phase ($\zeta_A = 0$). This test case, established by Fleckenstein and Bothe (2015), consider a bubble subjected to a gravitational field in an undersaturated liquid. It is based on the velocity field around a rigid sphere proposed by Hadamard (1911). The corresponding terminal velocity U_P of a rigid sphere with radius R is given by:

$$U_P = \frac{2}{3}\frac{\rho_l - \rho_g}{\mu_l} g R^2 \frac{1 + \mu_g/\mu_l}{2 + 3\mu_g/\mu_l}, \tag{49}$$

where g denotes the gravitational constant applied to the system. From this terminal velocity, Fleckenstein and Bothe (2015) proposed an evolution of the sphere radius over time, based on the Sherwood number Sh :

$$\dot{R}(t) = -\frac{H_A D_{A,l}}{2} \frac{\mathrm{Sh}\,(R(t))}{R(t)}. \tag{50}$$

This equation allows a 3D validation of the model by incorporating phase volume change into mass transfer in a bubble submitted to gravitational effects. In (Eq. 50), the Sherwood number Sh depends on the Reynolds number Re and the Schmidt number Sc. In flows involving variable-volume bubbles, the Reynolds number Re is defined by :

$$Re(t) = \frac{\rho_c U(t) 2R(t)}{\mu_c}, \tag{51}$$

where $U(t)$ denotes the magnitude of the barycentric velocity of the sphere. For this type of test case, a correlation for the Sherwood number Sh is defined through the Péclet number ($\mathrm{Pe} = \mathrm{ReSc}$) as (Fleckenstein and Bothe (2015)) :

$$\mathrm{Sh}(t) = 2 + 0.651 \frac{\mathrm{Pe}(t)^{1.72}}{1 + \mathrm{Pe}(t)^{1.22}}. \tag{52}$$

This expression is valid for $\mathrm{Re} \to 0$ and $\mathrm{Sc} \to \infty$ and is based on a numerical calculation of mass transfer in a spherical bubble, providing a good estimate for the Sherwood number.

A circular, pure gaseous phase with an initial diameter of $D_b^0 = L_{ref} = 4 \times 10^{-3}\,\mathrm{m}$ is immersed in an undersaturated liquid phase ($\zeta_A = 0$). The densities and viscosities of both phases are provided in Table 4. The values of the Henry's constant is $H_A = 2 \times 10^{-1}$ and the diffusion coefficient is $D_{A,l} = 1.48 \times 10^{-6}\,\mathrm{m}^2\,\mathrm{s}^{-1}$. These conditions correspond to a high Schmidt number of $Sc = 2.5 \times 10^2$, which justifies the use of (Eq. 52) since $Sc \gg 1$ and $\mathrm{Re} \to 0$. The surface tension force $\boldsymbol{f}_{\boldsymbol{\Sigma}}$ is calculated using Equation (25), with a surface tension coefficient of $\sigma = 6 \times 10^{-2}\,\mathrm{N}\,\mathrm{m}^{-1}$.

Additionally, to validate the shifted method presented in this study against the results reported by Gennari et al. (2022), a gravitational constant of $g = 8.92\,\mathrm{m}^2\,\mathrm{s}^{-1}$ is applied. This approach enables both quantitative and qualitative comparisons of bubble velocity, concentration drag length, and overall concentration distribution as documented in Gennari et al. (2022).

The numerical domain consists of a square with sides of length $l_u = 30L_{ref}$. A 2D axisymmetric domain is used in this study. This approach is adopted to reduce both simulation time and computational resource requirements. The mesh configuration combines a composite mesh along the horizontal direction x with a uniform mesh along the vertical direction y. In the horizontal direction x, the composite mesh transitions from a uniform mesh extending to $x = 4L_{ref}$ to an exponential mesh for the remaining domain. To achieve high-resolution velocity field measurements around the bubble, the mesh density is set to imposed 50 cells per diameter.

Table 4 – Phases properties in the rising bubble test cases.

Phase	Density [$\mathrm{kg\,m^{-3}}$]	Viscosity [$\mathrm{N\,s\,m^{-2}}$]	Diffusivity [$\mathrm{m^2\,s^{-1}}$]	Surface tension [$\mathrm{N\,m^{-1}}$]
liquid	1.245×10^3	4.6×10^{-1}	1.48×10^{-6}	6×10^{-2}
gas	1.2	1.8×10^{-5}	0	

In order to obtain comparable results with (Eq. 50), the simulation process is conducted in two distinct steps (Fleckenstein and Bothe (2015); Maes and Soulaine (2020); Gennari et al. (2022)) as illustrated in Fig. 10. The first step, spanning from $t = 0$ to $t = t_0$, solves the system of equations without source terms in (Eq. 20) and (Eq. 26). During this phase, mass transfer is simulated without phase volume changes to establish both a steady terminal velocity field and a concentration field around the bubble corresponding to this velocity field. The second step starts at $t = t_0$ with the activation of source terms in equations (Eq. 20) and (Eq. 26). This activation enables the simulation to account for phase volume changes associated with mass transfer.

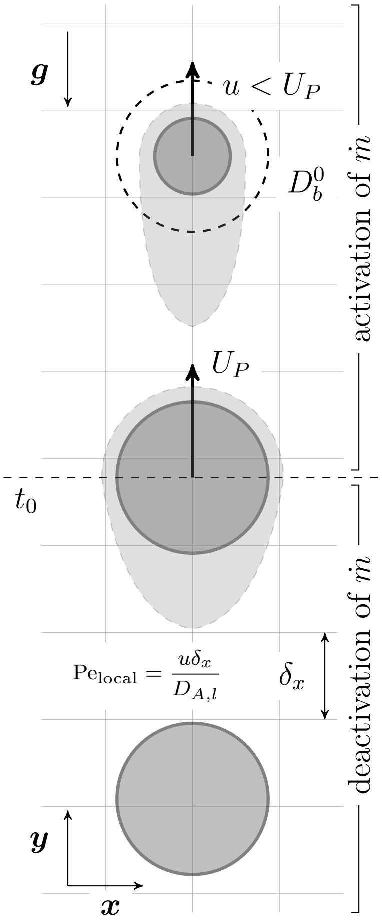

Figure 10 – Illustrations of the two steps during dissolution test case of mass transfer from a gas bubble in creeping flow.

The simulation is performed using a time step $\delta t = 1 \times 10^{-5}\,\mathrm{s}$. The reference time is set to $t_{\mathrm{ref}} = \sqrt{L_{ref}/g}$ and t_0 is computed with $t_0/t_{\mathrm{ref}} = 25$ as in Gennari et al. (2022) and the reference concentration is $\rho_{A,ref} = \rho_g$. We also define the local Péclet number as

$$\mathrm{Pe}_{\mathrm{local}} = \frac{u\delta_x}{D_{A,l}}, \tag{53}$$

where u represents the local advection velocity intensity and δ_x denotes the space step of the cell.

Nevertheless, to obtain results consistent with the semi-analytical solution (Eq. 50), an additional numerical velocity $\boldsymbol{u}_{\mathrm{ice}}$ (called interface concentration equilibrium velocity) is considered in place of $\boldsymbol{u_r}$ in (Eq. 15) and defined as $\boldsymbol{u}_{\mathrm{comp}}$ by (Eq. 19). Without this term, the simulation failed to respect the concentration discontinuity imposed by Henry's law at both the top and rear of the bubble, leading to supersaturation. A comparison between the normalized concentration profile at the front and rear of the bubble, with and without the interface concentration equilibrium velocity $\boldsymbol{u}_{\mathrm{ice}}$, is provided in Fig. 11 just before the second step of the simulation (*i.e.* before the activation of the interface displacement). This comparison clearly show that the interface is not at thermodynamic equilibrium without the terms involving $\boldsymbol{u}_{\mathrm{ice}}$.

With the use of this term the interface maintains its thermodynamic equilibrium during the dissolution phenomena with phase volume change as shown in Fig. 12. The simulation also accurately predicts the volume variation of the gas phase, as shown in Fig. 13, using the shifted and unshifted mass transfer rate methodologies, in agreement with no more than $0.8\,\%$ compared with the analytical solution (Eq. 50). A quantitative representation through a concentration map is provided in Fig. 14. Throughout the simulation, the bubble maintains its spherical shape as expected, and concentration gradients are similar with those reported in the literature Maes and Soulaine (2020) and Gennari et al. (2022). The terminal velocity of the bubble at t_0 is $U_P = 3.28 \times 10^{-2}\,\mathrm{m\,s^{-1}}$ which is close to the velocity predicted of $3.2 \times 10^{-2}\,\mathrm{m\,s^{-1}}$ by (Eq. 49). Moreover, at $(t - t_0)/t_{\mathrm{ref}} = -5$ and $(t - t_0)/t_{\mathrm{ref}} = 15$, the bubble position and the concentration drag length are similar with those presented in Gennari et al. (2022).

The interface concentration equilibrium velocity $\boldsymbol{u}_{\mathrm{ice}}$ is not used for maintaining a sharp interface as $\boldsymbol{u}_{\mathrm{comp}}$ (discussed in section 3.1) since the interface is very sharp during every simulations. It maintains thermodynamic equilibrium at the interface, as the competition

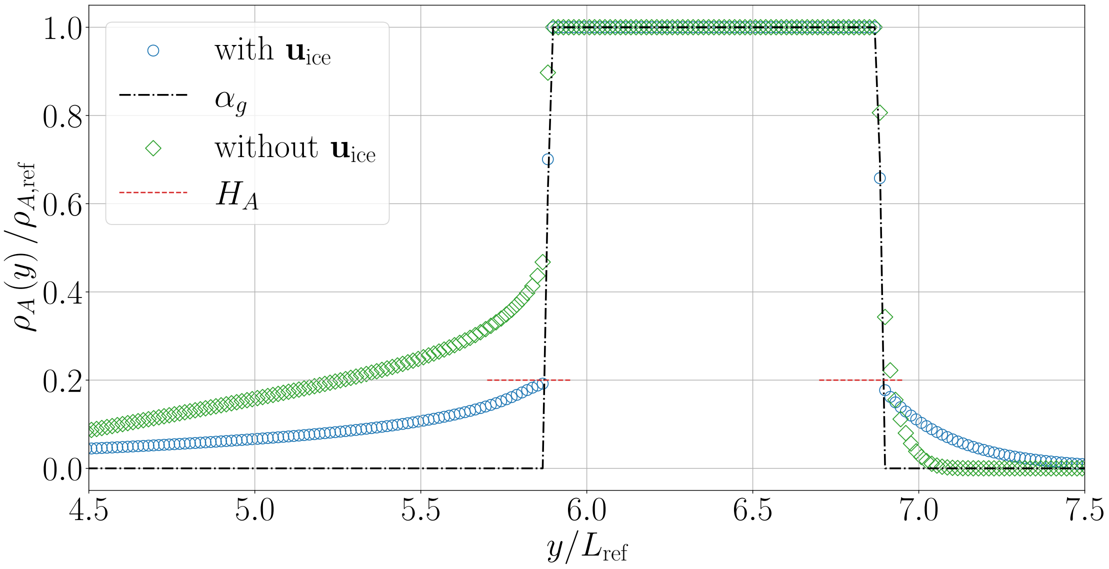

Figure 11 – Concentration profile along the vertical y-axis passing through bubble centre during dissolution phenomena without phase volume change at $(t - t_0)/t_{\text{ref}} = -5$ for high local Péclet number ($\text{Pe}_{\text{local}} > 1$). Comparison with (blue) and without (green) the interface concentration equilibrium velocity $\boldsymbol{u}_{\text{ice}}$. The value of the Henry's constant is $H_A = 2 \times 10^{-1}$ and the saturation ratio is $\zeta_A = 0$.

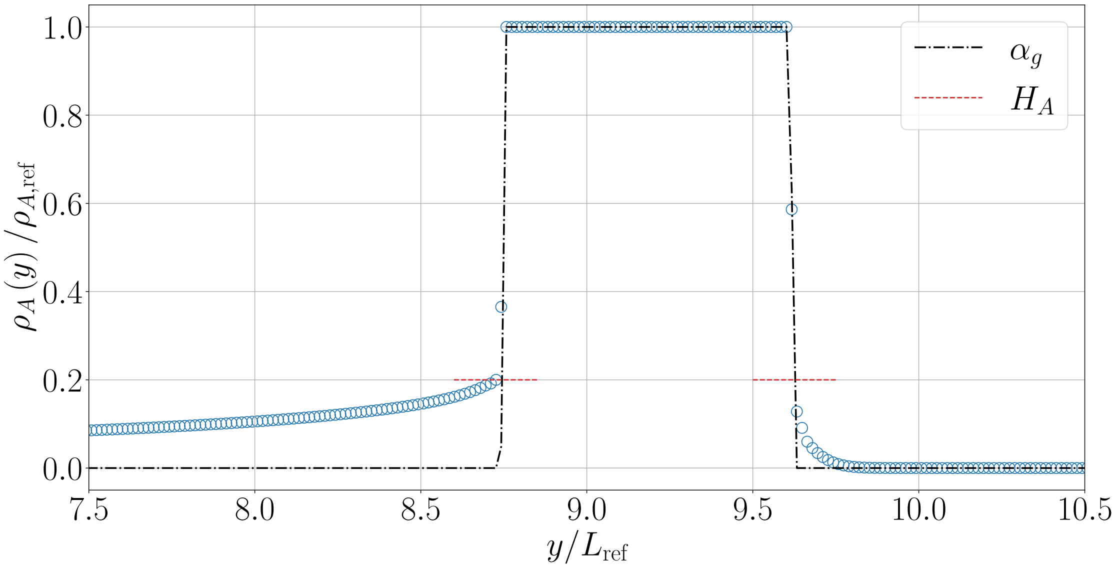

Figure 12 – Concentration profile along the vertical y-axis passing through bubble centre during dissolution phenomena with phase volume change at $(t - t_0)/t_{\text{ref}} = 15$ for high local Péclet number ($\text{Pe}_{\text{local}} > 1$). Results obtained with the interface concentration equilibrium velocity $\boldsymbol{u}_{\text{ice}}$. The value of the Henry's constant is $H_A = 2 \times 10^{-1}$ and the saturation ratio is $\zeta_A = 0$.

between the advection term $\nabla \cdot (\boldsymbol{u}\rho_i)$ and the CST flux $\nabla \cdot \boldsymbol{\phi_i}$ fails to impose this interface equilibrium. Note that this issue was encountered with multiple advection schemes, not only CICSAM. Advection schemes such as OS-CICSAM (Saincher and V (2022), explicit advection scheme), MSTACS (Anghan et al. (2021)), and even STACS (Darwish and Moukalled (2006)) produced the same results.

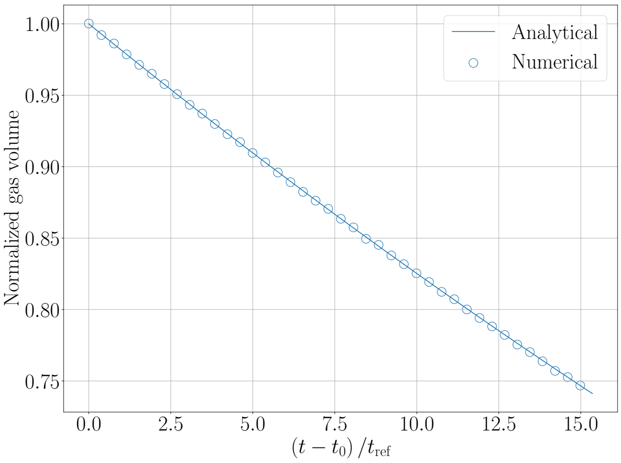

Figure 13 – Evolution of the bubble volume normalized by its initial value during the dissolution with diffusion coefficient $D_{A,l} = 1.48 \times 10^{-6}\,\mathrm{m^2\,s^{-1}}$, Henry's constant $H_A = 2 \times 10^{-1}$, and saturation ratio $\zeta_A = 0$. The interface concentration equilibrium velocity $\boldsymbol{u}_{\text{ice}}$ with $c_\alpha = 1.5$ is used in order to obtain these results for high local Péclet number ($\text{Pe}_{\text{local}} > 1$).

A discussion started by Yang et al. (2017), stated that when convection dominates diffusion locally near the interface, the CST method generates a large numerical error. They show that in order to capture the discontinuity at the interface accurately, the local Péclet number should respect

$$\text{Pe}_{\text{local}} < 0.5. \tag{54}$$

In simulations conducted without $\boldsymbol{u}_{\text{ice}}$, the local Péclet number is superior to 0.5 at both the front and rear of the bubble. It should be noted that reducing δ_x could achieve $\text{Pe}_{\text{local}} < 0.5$, however it significantly increases computational resource requirements.

To expand the discussion further, a two-phase transport in a 1D tube at infinite Péclet number was successfully conducted by Maes and Soulaine (2020) using the compressive velocity $\boldsymbol{u}_{\text{comp}}$ and by Zanutto et al. (2022b) without $\boldsymbol{u}_{\text{comp}}$ but by using CICSAM. However, in this test

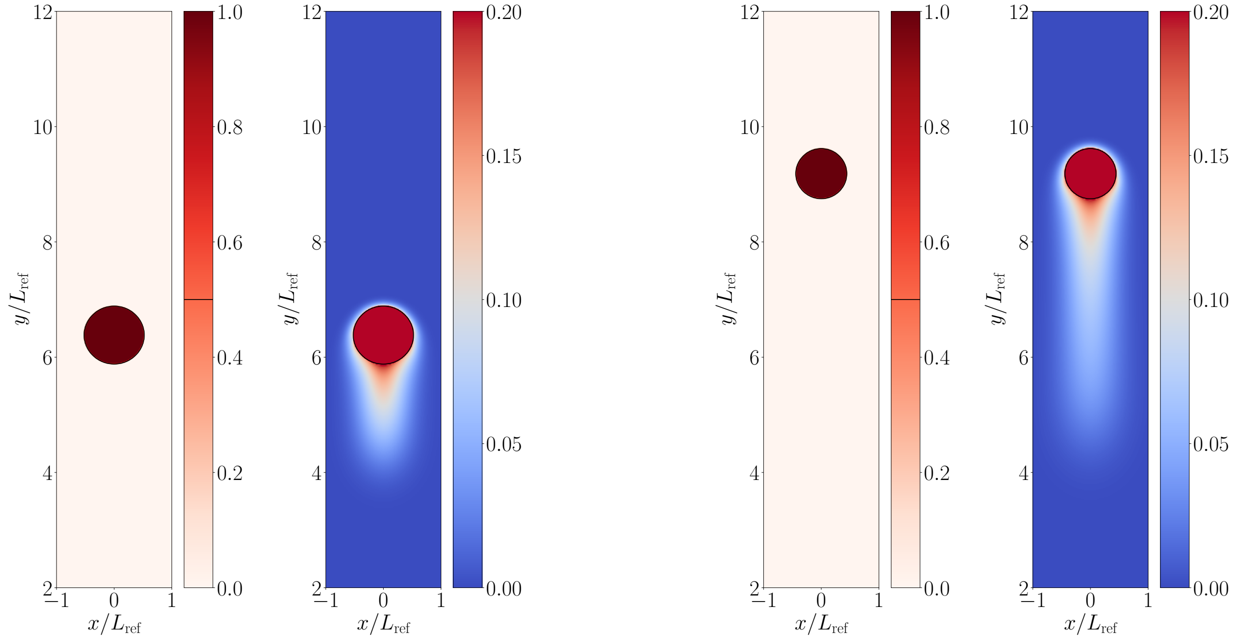

(a)

(b)

Figure 14 – Dissolution simulation of rising bubble subjected to gravity and undersaturated solution characterized by $\zeta_A = 0$ with a henry's coefficient $H_A = 2 \times 10^{-1}$ and a diffusion coefficient $D_{A,l} = 1.48 \times 10^{-6}\,\mathrm{m^2\,s^{-1}}$ (corresponding to high local Péclet number $\mathrm{Pe}_{\text{local}} > 1$). The volume fraction α_g and the normalized concentration map $\rho_A/\rho_{A,\text{ref}}$ are presented in the left and right respectively at (a) $(t - t_0)/t_{\text{ref}} = -5$ and (b) $(t - t_0)/t_{\text{ref}} = 15$. The contour of volume fraction is set up at $\alpha_g = 0.5$.

case, the mass transfer flux and the advective mass flux are perpendicular, as observed on the sides of the bubble where the concentration jump is accurately captured by the model without the terms involving $\boldsymbol{u}_{\text{ice}}$ (note that the local Péclet number is also inferior to 0.5 on these side). It can be supposed that, when collinear, these two fluxes impact the accurate captures of the concentration jump at the interface. Indeed, when a constant velocity (along the y-axis) is introduced into the domain for the 1D-dissolution case in section 5.1 and the 1D-precipitation case in section 6.2, the same issue arises. This confirms that collinear fluxes impact the accurate representation of concentration jumps at the interface for high Péclet numbers.

To further investigate this phenomenon, we conducted an additional simulation using a higher diffusion coefficient $D_{A,l} = 2.22 \times 10^{-5}\,\mathrm{m^2\,s^{-1}}$, which ensured that $\mathrm{Pe}_{\text{local}} < 0.5$ (Eq. 54) throughout the entire domain. The dissolving kinetics, presented in Fig. 15, were obtained without incorporating terms involving the interface concentration equilibrium velocity $\boldsymbol{u}_{\text{ice}}$. Notably, despite the absence of these terms, the numerical results demonstrate excellent agreement with the analytical solution. As shown in Fig. 15, between $(t - t_0)/t_{\text{ref}} = 0$ and $t/t_{\text{ref}} = 15$ there is huge volume variation.

The normalised concentration profiles along the y-axis passing through the bubble centre, as illustrated in Fig. 16, demonstrate that the interface equilibrium is maintained throughout the simulation of the rising bubble under low local Péclet number conditions. A quantitative representation of the concentration distribution and bubble position is presented in Fig. 17. Notably, the bubble maintains its spherical shape throughout the dissolution process.

The comparative analysis between simulations using $D_{A,l} = 1.48 \times 10^{-6}\,\mathrm{m^2\,s^{-1}}$ with $\boldsymbol{u}_{\text{ice}}$ and $D_{A,l} = 2.22 \times 10^{-5}\,\mathrm{m^2\,s^{-1}}$ without $\boldsymbol{u}_{\text{ice}}$ (Fig. 11, Fig. 12 and Fig. 16) reveals that the local Péclet number significantly influences the calculation of the thermodynamic equilibrium at the interface. It is important to mention that the use of $\boldsymbol{u}_{\text{ice}}$ influence the kinetics of the interface.

7.2 Precipitation

Finally, the 3D dynamic simulation of the growth of a rising bubble subjected to gravity is study in order to exhibit the relevance of the shifted numerical methodology proposed in this study in solving precipitation phenomena with the one-field approach. In this case, the set up is the same as the one used for the dissolving rising bubble studied in section 7.1. A

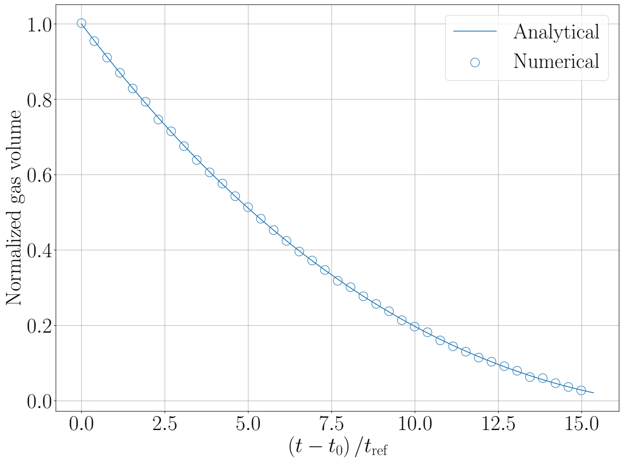

Figure 15 – Evolution of the bubble volume normalized by its initial value during the dissolution with diffusion coefficient $D_{A,l} = 2.22 \times 10^{-5}\,\text{m}^2\,\text{s}^{-1}$ (corresponding to low local Péclet number $\text{Pe}_{\text{local}} < 0.5$), Henry's constant $H_A = 2 \times 10^{-1}$, and saturation ratio $\zeta_A = 0$. Results obtained without the interface concentration equilibrium velocity $\boldsymbol{u}_{\text{ice}}$.

Henry coefficient of $H_A = 2 \times 10^{-1}$ is used with an initial concentration of the continuous phase of $\rho^0_{A,l} = 4.8 \times 10^{-1}\,\text{kg}\,\text{m}^{-3}$ corresponding to a saturation ratio $\zeta_A = 2$. A diffusion coefficient $D_{A,l} = 2.22 \times 10^{-5}\,\text{m}^2\,\text{s}^{-1}$ is used in order to achieve $\text{Pe}_{\text{local}} < 0.5$ to avoid both inaccurate concentration discontinuity at the interface and the use of $\boldsymbol{u}_{\text{ice}}$ as demonstrate in section 7.1.

Rather than dividing the simulation into two distinct steps (step 1: without phase volume change and step 2: with phase volume change) as made previously, the current simulation is conducted by immediately activating the phase volume change. Specifically, the source terms accounting for phase volume variation in equations (Eq. 20) and (Eq. 26) are activated from the beginning of the simulation.

Fig. 18 shows the results, of this study where the normalized volume of the dispersed phase is plotted as a function of the time after a total simulated physical time of 0.2 s. The bubble exhibits spherical shape during the simulation time as it was the case in the dissolution cases. Moreover, a comparison between the numerical and empirical mass transfer coefficient k_A is conducted. Numerically, the mass transfer coefficient is computed as

$$k_A = \frac{\boldsymbol{n}_{\boldsymbol{\Sigma}} \cdot \boldsymbol{\nabla}\left(D_{A,l}\rho_A\right)|_{\alpha_g=0.5}}{\rho^0_{A,l} - \rho_{A,g}}. \tag{55}$$

The empirical mass transfer coefficient $k_{A,\text{emp}}$ is computed though the Sherwood number with

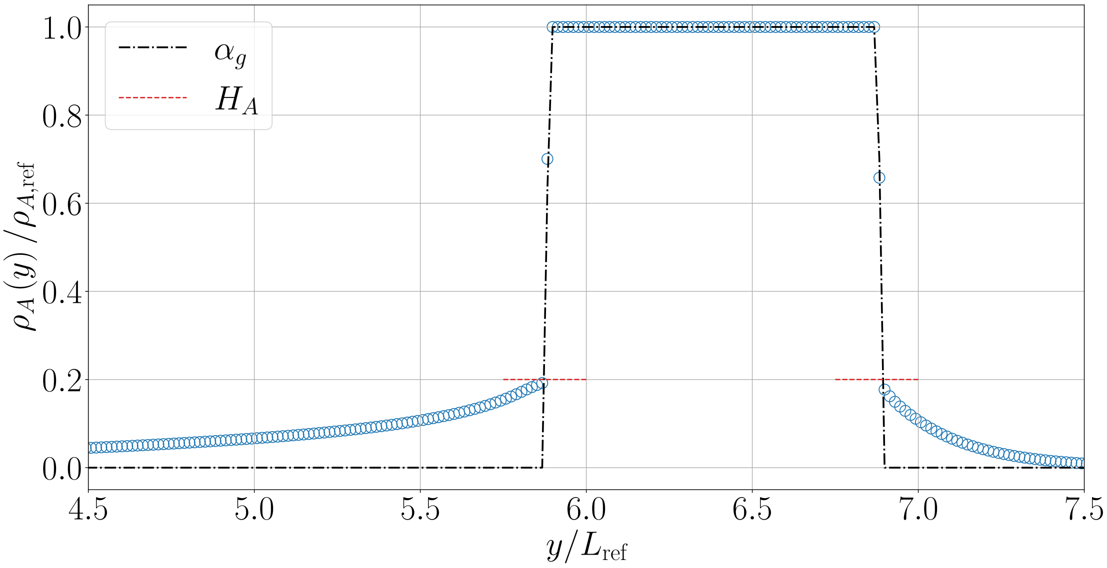

(a)

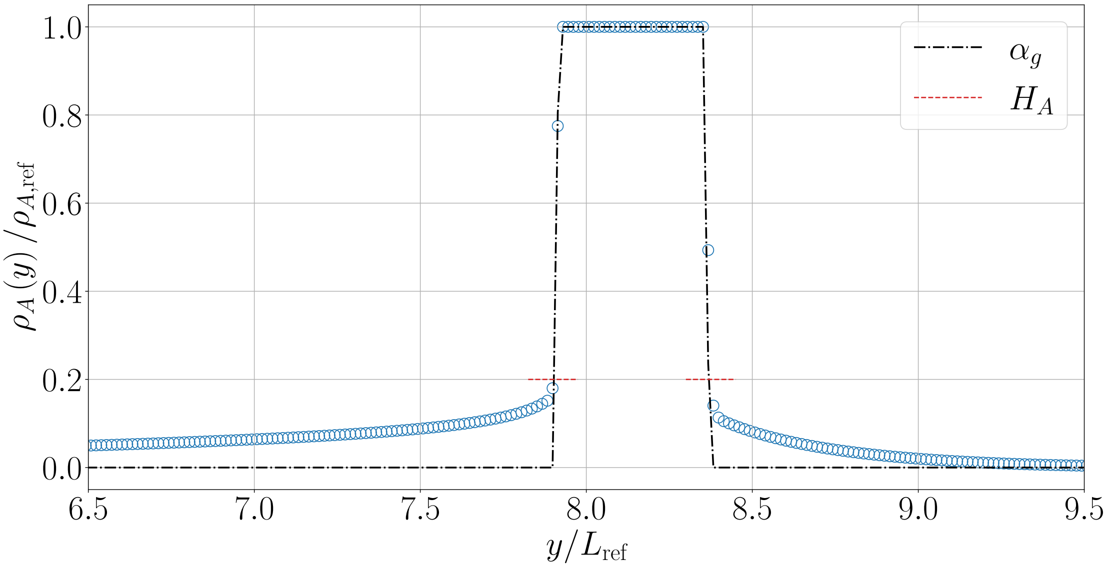

(b)

Figure 16 – Concentration profile along the y-axis passing through bubble centre during rapid dissolution phenomena at (a) $(t - t_0)/t_{\mathrm{ref}} = -5$ without phase volume change and (b) $(t-t_0)/t_{\mathrm{ref}} = 15$ with phase volume change. Results obtained without the interface concentration equilibrium velocity $\boldsymbol{u}_{\mathrm{ice}}$ for low local Péclet number ($\mathrm{Pe}_{\mathrm{local}} < 0.5$). The value of the Henry's constant is $H_A = 2 \times 10^{-1}$ and the saturation ratio is $\zeta_A = 0$.

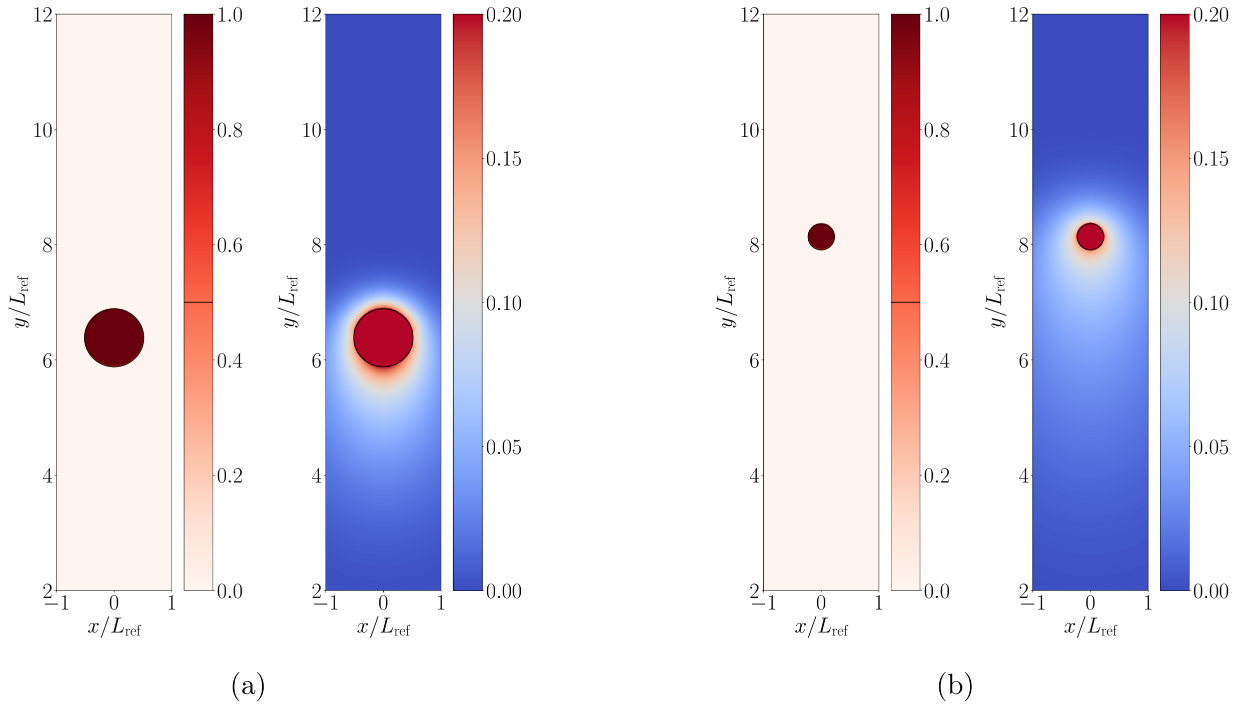

(a) (b)

Figure 17 – Rapid dissolution simulation of rising bubble subjected to gravity and undersaturated solution characterized by $\zeta_A = 0$ with a henry's coefficient $H_A = 2 \times 10^{-1}$ and a diffusion coefficient $D_{A,l} = 2.22 \times 10^{-5}\,\mathrm{m}^2\,\mathrm{s}^{-1}$ (corresponding to low local Péclet number $\mathrm{Pe}_{\text{local}} < 0.5$). The volume fraction α_g and the normalized concentration map $\rho_A/\rho_{A,\text{ref}}$ are presented in the left and right respectively at (a) $(t - t_0)/t_{\text{ref}} = -5$ and (b) $(t - t_0)/t_{\text{ref}} = 15$. The contour of volume fraction is set up at $\alpha_g = 0.5$.

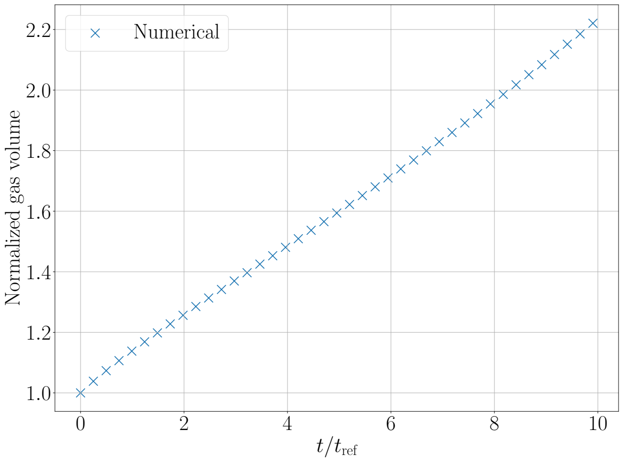

Figure 18 – Evolution of the bubble volume normalized by its initial value during the precipitation with diffusion coefficient $D_{A,l} = 2.22 \times 10^{-5}\,\mathrm{m}^2\,\mathrm{s}^{-1}$ (corresponding to low local Péclet number $\mathrm{Pe}_{\text{local}} < 0.5$), Henry's constant $H_A = 2 \times 10^{-1}$, and saturation ratio $\zeta_A = 2$. Results obtained without the interface concentration equilibrium velocity $\boldsymbol{u}_{\text{ice}}$.

$$Sh_{\mathrm{emp}} = \frac{k_{A,\mathrm{emp}} L_{\mathrm{ref}}}{D_{A,l}}, \tag{56}$$

where the values of the Sherwood number is obtain from (Eq. 52). The mass transfer coefficients, calculated from both empirical correlations and numerical simulations, are presented in Table 5.

Table 5 – Comparison between mass transfer coefficients, calculated from both empirical correlations and numerical simulations.

t/t_{ref}	$k_{A,\mathrm{emp}}\,[\mathrm{m^2\,s^{-1}}]$	$k_{A,\mathrm{num}}\,[\mathrm{m^2\,s^{-1}}]$
5	4.24×10^{-2}	3.67×10^{-2}
10	3.82×10^{-2}	3.25×10^{-2}

The shifted method employed in this study produces a mass transfer coefficient of the same order of magnitude as that derived from empirical correlations with 15% errors. This demonstrates that the model successfully captures the kinetics of the precipitation phenomenon. The consistency between the calculated mass transfer coefficients, coupled with thorough validation against previous test cases, supports our hypothesis that the normalised dispersed phase volume variation accurately reflects the modelled physical phenomenon. A quantitative representation of the concentration distribution is provided in Fig. 19, and the concentration profile at $t/t_{\mathrm{ref}} = 10$ presented in Fig. 20 demonstrates that the interface maintains its thermodynamic equilibrium throughout the simulation without the use of $\boldsymbol{u}_{\mathrm{ice}}$.

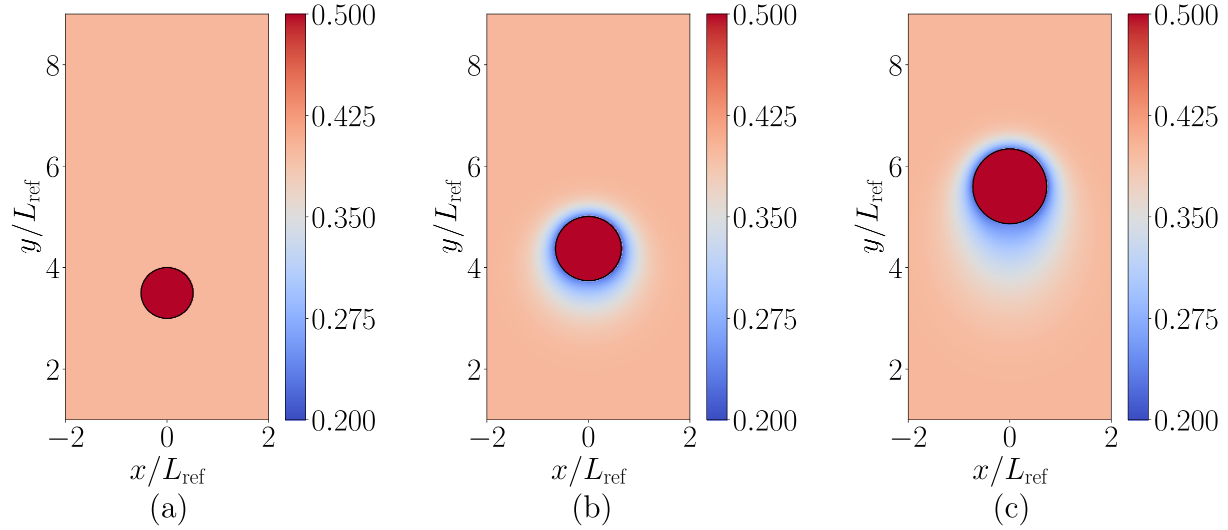

(a) (b) (c)

Figure 19 – Precipitation simulation of rising bubble subjected to gravity and supersaturated solution characterized by $\zeta_A = 2$ with a henry's coefficient $H_A = 2 \times 10^{-1}$ and a diffusion coefficient $D_{A,l} = 2.22 \times 10^{-5}\,\mathrm{m^2\,s^{-1}}$ (corresponding to low local Péclet number $\mathrm{Pe}_{\mathrm{local}} < 0.5$). Normalized concentration map $\rho_A/\rho_{A,\mathrm{ref}}$ are presented in function of the time : (a) $t/t_{\mathrm{ref}} = 0$, (b) $t/t_{\mathrm{ref}} = 5$ and (c) $t/t_{\mathrm{ref}} = 10$. The contour of volume fraction is set up at $\alpha_g = 0.5$. Results obtained without the interface concentration equilibrium velocity $\boldsymbol{u}_{\mathrm{ice}}$.

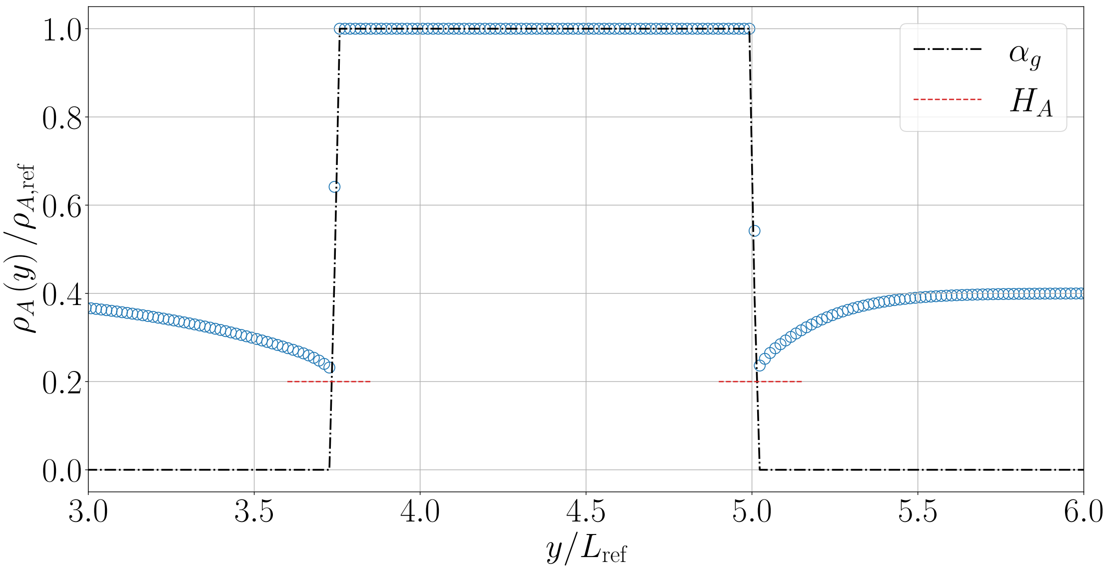

Figure 20 – Concentration profile along the vertical y-axis passing through bubble centre during precipitation phenomena with phase volume change at $t/t_{\mathrm{ref}} = 5$. Results obtained without the interface concentration equilibrium velocity $\boldsymbol{u}_{\mathrm{ice}}$ for low local Péclet number ($\mathrm{Pe}_{\mathrm{local}} < 0.5$). The value of the Henry's constant is $H_A = 2 \times 10^{-1}$ and the saturation ratio is $\zeta_A = 2$.

8 Conclusion

In this work we implemented the single-field C-CST formulation developed by Maes and Soulaine (2020) within the `Notus` open-source CFD software, employing a Volume of Fluid (VOF) approach based on Ubbink and Issa (1999) Compressive Interface Capturing Scheme for Arbitrary Meshes (CICSAM). While existing single-field methodologies (Maes and Soulaine (2020), Zanutto et al. (2022b)) have demonstrated success in modelling dissolution phenomena, the simulation of precipitation processes has remained an unaddressed challenge. Our study reveals that state-of-the-art discretisation approaches in single-field literature prove inadequate for accurately representing precipitation phenomena. To overcome these limitations, we introduced a shifted discretisation methodology for source terms implying mass transfer rate. This approach, developed by extending the work of Malan et al. (2021) and Gennari et al. (2022), establishes a framework that enables both modelling and simulation of precipitation phenomena within the single-field context.

Additionally, our contribution extends beyond implementation to theoretical foundation, presenting new analytical solutions for both one-dimensional and two-dimensional static precipitation phenomena based on the three-dimensional solution developed by Scriven (1959). This comprehensive approach establishes complete dimensional (1D, 2D and 3D) benchmarks that account for phase volume changes during precipitation, addressing a significant gap in the existing literature.

Comprehensive validation across multiple scenarios demonstrates the robustness of our approach. For static cases, the method shows excellent agreement with established analytical solutions across multiple dimensions: the one-dimensional solutions of Crank (1979), the three-dimensional approximative solution of Epstein and Plesset (1950) for dissolution phenomena, and Scriven (1959) three-dimensional solution for precipitation. Additionally, our work validates successfully against newly developed analytical solutions for both one-dimensional and two-dimensional static precipitation scenarios. This study achieves a significant step by bringing single-field approaches to parity with two-field methods in modelling both dissolution and precipitation phenomena.

In dynamic scenarios involving gas bubbles in creeping flow, our numerical results demonstrate strong alignment with Fleckenstein and Bothe (2015) semi-analytical solutions across various configurations. However, an important limitation emerged when replicating high Schmidt number conditions (Sc=250): maintaining thermodynamic equilibrium at the interface required the implementation of an additional velocity term, $\boldsymbol{u_{ice}}$. While this modification proves unnecessary for cases with lower Péclet numbers ($\mathrm{Pe}_{\mathrm{local}} < 0.5$), it raises important questions about concentration jump at the interface within the single-field framework for high Péclet numbers. This particular aspect of the methodology requires further investigation, as our analysis remains inconclusive and opens future research in competition between advection and diffusion velocities in the context of single-field mass transfer with phase volume change.

In addition to these investigations, our future work objectives also include validating the proposed method against experimental setups. Specifically, we plan to validate our approach using microfluidic channels or in situ microspectroscopy for both low-pressure (Tan et al. (2012)) and high-pressure conditions (Kuhn and Jensen (2012), Deleau et al. (2020)).

Acknowledgments

The authors would like to thank the Agence Nationale de la Recherche (Grant No. ANR-21-CE50-0021) for financial support and the MCIA (Mésocentre de Calcul Intensif Aquitaine).

References

Aboulhasanzadeh, B., Thomas, S., Taeibi-Rahni, M., and Tryggvason, G. (2012). Multiscale computations of mass transfer from buoyant bubbles. *Chemical Engineering Science*, 75:456–467.

Anghan, C., Bade, M. H., and Banerjee, J. (2021). A modified switching technique for advection and capturing of surfaces. *Applied Mathematical Modelling*, 92:349–379.

Badillo, A. (2012). Quantitative phase-field modeling for boiling phenomena. *Phys. Rev. E*, 86:041603.

Balcázar-Arciniega, N., Antepara, O., Rigola, J., and Oliva, A. (2019). A level-set model for mass transfer in bubbly flows. *International Journal of Heat and Mass Transfer*, 138:335–356.

Bäumler, K. (2014). *Simulation of single drops with variable interfacial tension.* PhD thesis, Erlangen, Friedrich-Alexander-Universität Erlangen-Nürnberg (FAU), Diss., 2014.

Brackbill, J., Kothe, D., and Zemach, C. (1992). A continuum method for modeling surface tension. *Journal of Computational Physics*, 100(2):335–354.

Crank, J. (1979). *The Mathematics of Diffusion.* Oxford science publications. Clarendon Press.

Darwish, M. and Moukalled, F. (2006). Convective schemes for capturing interfaces of free-surface flows on unstructured grids. *Numerical Heat Transfer, Part B: Fundamentals*, 49(1):19–42.

Deising, D., Marschall, H., and Bothe, D. (2016). A unified single-field model framework for volume-of-fluid simulations of interfacial species transfer applied to bubbly flows. *Chemical Engineering Science*, 139:173–195.

Deleau, T., Fechter, M., Letourneau, J.-j., Camy, S., Aubin, J., Braeuer, A. S., and Espitalier, F. (2020). Determination of mass transfer coefficients in high-pressure two-phase flows in capillaries using Raman spectroscopy. *Chemical Engineering Science*, 228:1–15/115960.

Deshpande, K. B. and Zimmerman, W. B. (2006). Simulations of mass transfer limited reaction in a moving droplet to study transport limited characteristics. *Chemical Engineering Science*, 61(19):6424–6441.

Duda, J. and Vrentas, J. (1971). Heat or mass transfer-controlled dissolution of an isolated sphere. *International Journal of Heat and Mass Transfer*, 14(3):395–407.

Duncan, P. B. and Needham, D. (2004). Test of the epstein-plesset model for gas microparticle dissolution in aqueous media: Effect of surface tension and gas undersaturation in solution. *Langmuir*, 20(7):2567–2578. PMID: 15835125.

Epstein, P. S. and Plesset, M. S. (1950). On the Stability of Gas Bubbles in Liquid-Gas Solutions. *The Journal of Chemical Physics*, 18(11):1505–1509.

Farsoiya, P. K., Popinet, S., and Deike, L. (2021). Bubble-mediated transfer of dilute gas in turbulence. *Journal of Fluid Mechanics*, 920.

Fleckenstein, S. and Bothe, D. (2015). A volume-of-fluid-based numerical method for multi-component mass transfer with local volume changes. *Journal of Computational Physics*, 301:35–58.

Gennari, G., Jefferson-Loveday, R., and Pickering, S. J. (2022). A phase-change model for diffusion-driven mass transfer problems in incompressible two-phase flows. *Chemical Engineering Science*, 259:117791.

Goda, K. (1979). A multistep technique with implicit difference schemes for calculating two- or three-dimensional cavity flows. *Journal of Computational Physics*, 30(1):76–95.

Graveleau, M., Soulaine, C., and Tchelepi, H. A. (2017). Pore-scale simulation of interphase multicomponent mass transfer for subsurface flow. *Transport in Porous Media*, 120:287–308.

Hadamard, J. (1911). Mouvement permanent lent d'une sphere liquid et visqueuse dans un liquid visqueux. *(No Title)*, 152:1735.

Hardt, S. and Wondra, F. (2008). Evaporation model for interfacial flows based on a continuum-field representation of the source terms. *Journal of Computational Physics*, 227:5871–5895.

Haroun, Y., Legendre, D., and Raynal, L. (2010). Volume of fluid method for interfacial reactive mass transfer: Application to stable liquid film. *Chemical Engineering Science*, 65:2896–2909.

Hayashi, K., Hosoda, S., Tryggvason, G., and Tomiyama, A. (2014). Effects of shape oscillation on mass transfer from a taylor bubble. *International Journal of Multiphase Flow*, 58:236–245.

Henry, W. and Banks, J. (1803). Experiments on the quantity of gases absorbed by water, at different temperatures, and under different pressures. *Philosophical Transactions of the Royal Society of London*, 93:29–274.

Hirt, C. and Nichols, B. (1981). Volume of fluid (vof) method for the dynamics of free boundaries. *Journal of Computational Physics*, 39:201–225.

Khinast, J. G., Koynov, A. A., and Leib, T. M. (2003). Reactive mass transfer at gas–liquid interfaces: impact of micro-scale fluid dynamics on yield and selectivity of liquid-phase cyclohexane oxidation. *Chemical Engineering Science*, 58(17):3961–3971.

Kuhn, S. and Jensen, K. F. (2012). A ph-sensitive laser-induced fluorescence technique to monitor mass transfer in multiphase flows in microfluidic devices. *Industrial & Engineering Chemistry Research*, 51:8999 – 9006.

Lehrenfeld, C. (2015). *On a space-time extended finite element method for the solution of a class of two-phase mass transport problems*. PhD thesis, Universitätsbibliothek der RWTH Aachen.

Leonard, B. P. (1991). The ultimate conservative difference scheme applied to unsteady one-dimensional advection. *Computer Methods in Applied Mechanics and Engineering*, 88:17–74.

Maes, J. and Soulaine, C. (2018). A new compressive scheme to simulate species transfer across fluid interfaces using the volume-of-fluid method. *Chemical Engineering Science*, 190:405–418.

Maes, J. and Soulaine, C. (2020). A unified single-field volume-of-fluid-based formulation for multi-component interfacial transfer with local volume changes. *Journal of Computational Physics*, 402.

Malan, L., Malan, A., Zaleski, S., and Rousseau, P. (2021). A geometric vof method for interface resolved phase change and conservative thermal energy advection. *Journal of Computational Physics*, 426:109920.

Marschall, H., Hinterberger, K., Schüler, C., Habla, F., and Hinrichsen, O. (2012). Numerical simulation of species transfer across fluid interfaces in free-surface flows using openfoam. *Chemical Engineering Science*, 78:111–127.

Notus (2024). Notus computational fluid dynamics, v0.6.0. *[https://notus-cfd.org/]*.

Palmore, J. and Desjardins, O. (2019). A volume of fluid framework for interface-resolved simulations of vaporizing liquid-gas flows. *Journal of Computational Physics*, 399:108954.

Perrier, H., Denner, F., Eaton, M. D., and van Wachem, B. G. (2019). On the numerical modelling of corium spreading using volume-of-fluid methods. *Nuclear Engineering and Design*, 345:216–232.

Popinet, S. (2009). An accurate adaptive solver for surface-tension-driven interfacial flows. *Journal of Computational Physics*, 228(16):5838–5866.

Radl, S., Koynov, A., Tryggvason, G., and Khinast, J. G. (2008). Dns-based prediction of the selectivity of fast multiphase reactions: Hydrogenation of nitroarenes. *Chemical Engineering Science*, 63(12):3279–3291.

Rusche, H. (2002). Computational fluid dynamics of dispersed two-phase flow at high phase fractions. *Ph. D. thesis, University of London.*

Saincher, S. and V, S. (2022). An efficient operator-split cicsam scheme for three-dimensional multiphase-flow problems on cartesian grids. *Computers and Fluids*, 240.

Scapin, N., Costa, P., and Brandt, L. (2020). A volume-of-fluid method for interface-resolved simulations of phase-changing two-fluid flows. *Journal of Computational Physics*, 407.

Scardovelli, R. and Zaleski, S. (1999). Direct numerical simulation of free-surface and interfacial flow. *Annu. Rev. Fluid Mech.*, 31.

Schulz, A., Wecker, C., Inguva, V., Lopatin, A. S., and Kenig, E. Y. (2022). A plic-based method for species mass transfer at free fluid interfaces. *Chemical Engineering Science*, 251:117357.

Scriven, L. (1959). On the dynamics of phase growth. *Chemical Engineering Science*, 10(1):1–13.

Slattery, J. C. (1999). *Advanced Transport Phenomena.* Cambridge Series in Chemical Engineering. Cambridge University Press.

Sussman, M., Smereka, P., and Osher, S. (1994). A level set approach for computing solutions to incompressible two-phase flow. *Journal of Computational Physics*, 114(1):146–159.

Tan, J., Lu, Y., Xu, J., and Luo, G. (2012). Mass transfer characteristic in the formation stage of gas–liquid segmented flow in microchannel. *Chemical Engineering Journal*, 185-186:314–320.

Taqieddin, A., Liu, Y., Alshawabkeh, A. N., and Allshouse, M. R. (2020). Computational modeling of bubbles growth using the coupled level set—volume of fluid method. *Fluids*, 5(3).

Taylor, R. and Krishna, R. (1993). *Multicomponent mass transfer*, volume 2. John Wiley & Sons.

Tourbier, A., Gamet, L., Béard, P., Michel, T., Aubin, J., and Jasak, H. (2024). A consistent methodology to transport a passive scalar with the geometric volume-of-fluid method isoadvector. *Journal of Computational Physics*, 513:113198.

Tryggvason, G., Bunner, B., Esmaeeli, A., Juric, D., Al-Rawahi, N., Tauber, W., Han, J., Nas, S., and Jan, Y.-J. (2001). A front-tracking method for the computations of multiphase flow. *Journal of Computational Physics*, 169(2):708–759.

Ubbink, O. and Issa, R. (1999). A method for capturing sharp fluid interfaces on arbitrary meshes. *Journal of Computational Physics*, 153(1):26–50.

Vachaparambil, K. J. and Einarsrud, K. E. (2020). Numerical simulation of bubble growth in a supersaturated solution. *Applied Mathematical Modelling*, 81:690–710.

Wang, J., Lu, P., Wang, Z., Yang, C., and Mao, Z.-S. (2008). Numerical simulation of unsteady mass transfer by the level set method. *Chemical Engineering Science*, 63(12):3141–3151.

Wang, Y., Hu, X., Cao, Z., and Guo, L. (2016). Investigations on bubble growth mechanism during photoelectrochemical and electrochemical conversions. *Colloids and Surfaces A: Physicochemical and Engineering Aspects*, 505:86–92.

Weber, P. S., Marschall, H., and Bothe, D. (2017). Highly accurate two-phase species transfer based on ale interface tracking. *International Journal of Heat and Mass Transfer*, 104:759–773.

Weller, H. G. (2008). A new approach to vof-based interface capturing methods for incompressible and compressible flow. *OpenCFD Ltd., Report TR/HGW*, 4:35.

Yang, C. and Mao, Z.-S. (2005). Numerical simulation of interphase mass transfer with the level set approach. *Chemical Engineering Science*, 60(10):2643–2660.

Yang, L., Nieves-Remacha, M. J., and Jensen, K. F. (2017). Simulations and analysis of multiphase transport and reaction in segmented flow microreactors. *Chemical Engineering Science*, 169:106–116.

Yu, H. and Leung, J. Y. (2025). A consistent interphase mass transfer method and level-set formulation for incompressible two-phase flows. *Chemical Engineering Science*, 306:121256.

Zalesak, S. T. (1979). Fully multidimensional flux-corrected transport algorithms for fluids. *Journal of Computational Physics*, 31(3):335–362.

Zanutto, C. P., Evrard, F., van Wachem, B., Denner, F., and Paladino, E. E. (2022a). Modeling interfacial mass transfer of highly non-ideal mixtures using an algebraic vof method. *Chemical Engineering Science*, 251.

Zanutto, C. P., Paladino, E. E., Evrard, F., van Wachem, B., and Denner, F. (2022b). Modeling of interfacial mass transfer based on a single-field formulation and an algebraic vof method considering non-isothermal systems and large volume changes. *Chemical Engineering Science*, 247.

Zener, C. (1949). Theory of growth of spherical precipitates from solid solution. *Journal of Applied Physics*, 20(10):950–953.

Appendix A. Growth of a gas bubble by mass transfer

This appendix provides a proof of the analytical solution (Eq. 45) used in section 6 to validate the proposed model and its implementation. We consider the growth of a gas bubble caused by the precipitation of a chemical species A in a supersaturated liquid solution of A in a solvent B. Following the proof of the spherically symmetric solution (3D) derived in Scriven (1959), we develop mirror symmetric (1D) and axially symmetric (2D) solutions where the bubble growth is driven solely by mass transfer.

In the following, we consider the n-dimensional problem, where $n \in [\![1, 3]\!]$ characterizes the type of symmetry and invariance. The case $n = 1$ corresponds to mirror symmetry, where the solution remains invariant under translation in any direction parallel to the plane of symmetry. For $n = 2$, the problem exhibits axial symmetry, implying that the solution is invariant under both rotation around the axis and translation along it. Finally, for $n = 3$, the system possesses spherical symmetry, meaning that the solution remains unchanged under any rotation around the origin. This particular case has previously been derived by Scriven (1959). Owing to these symmetries, only a single spatial coordinate, denoted r, is required, representing the shortest distance from any point to the object defining the symmetry (plane, axis, or point). The interface between the gas phase g and the liquid phase ℓ is denoted by Σ and is defined as the set of points located at a distance $r = R(t)$ at time t. Its normal vector is denoted by $\boldsymbol{n}_\Sigma$. The geometric configuration is illustrated in Fig. 21.

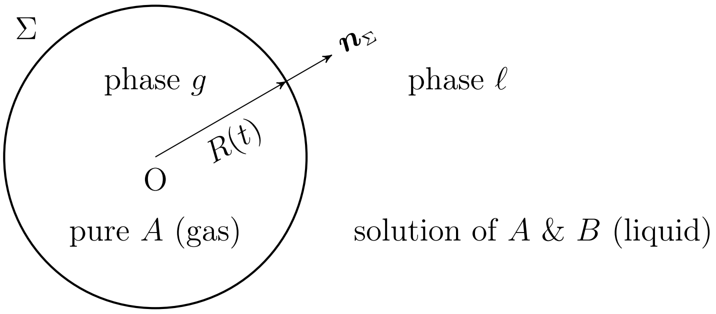

Figure 21 – Cross-section of the gas bubble for the axially (2D) or spherically (3D) symmetric cases. The gas bubble (phase g), bounded by the surface Σ, is composed of a pure chemical species A that grows in a supersaturated liquid solution of A in B (phase ℓ).

Our goal is to establish the evolution law governing the bubble radius $R(t)$ and the mass concentration of species A over time subject to the following hypotheses:

1. The gas phase g consists solely of species A with a constant mass concentration ρ_A.
2. The densities of both the gas and liquid phases are constant and denoted by ρ_g and ρ_l, respectively.

3. The velocity within the gas phase g is zero.
4. The bubble growth is driven exclusively by mass transfer. For instance, the effects of surface tension will be neglected.
5. The mass concentration of species A at the interface Σ remains constant and is denoted by $\rho_{A,l}^{*}$.
6. At $r \to \infty$, the mass concentration of species A is a constant denoted by $\rho_{A,l}^{\infty}$.

In the following, the mass concentration fields of species A and B are denoted by $\rho_A(r,t)$ and $\rho_B(r,t)$, respectively. By hypothesis 1, $\rho_B(r,t) = 0$ for all $r < R(t)$. Furthermore, by hypothesis 2, the densities of both phases are related to the mass concentrations as follows:

$$\rho_g = \rho_A(r,t) \quad \text{and} \quad \rho_l = \rho_A(r,t) + \rho_B(r,t). \tag{57}$$

Mass conservation in both phases is expressed as

$$\frac{\partial \rho}{\partial t} + \nabla \cdot (\rho \boldsymbol{u}) = 0. \tag{58}$$

Applying hypothesis 2 and considering spatial invariance, this equation simplifies to

$$\frac{1}{r^{n-1}} \frac{\partial r^{n-1} u(r,t)}{\partial r} = 0, \tag{59}$$

where $u(r,t)$ represents the velocity along the normal direction. The velocity components in all other directions are zero. The jump condition for the density across the interface Σ is given by

$$-\rho_g \dot{R}(t) = \rho_l \big(u\big(R(t),t\big) - \dot{R}(t)\big), \tag{60}$$

where $\dot{R}(t)$ denotes the time derivative of the bubble radius corresponding to the interface velocity. Introducing the following notation simplifies this expression:

$$\varepsilon \dot{R}(t) = u\big(R(t),t\big) \quad \text{with} \quad \varepsilon = \frac{\rho_l - \rho_g}{\rho_l}. \tag{61}$$

Solving (Eq. 59) using the jump condition (Eq. 61) gives the relationship between the velocity field and the bubble radius:

$$r^{n-1} u(r,t) = \begin{cases} 0 & \text{if } r < R(t) \\ \varepsilon R^{n-1}(t) \dot{R}(t) & \text{otherwise} \end{cases}. \tag{62}$$

Notably, if $\rho_g = \rho_l$, the velocity in both phases is identically zero.

In each phase, the mass conservation of species A is governed by the equation

$$\frac{\partial \rho_A}{\partial t} + \nabla \cdot (\rho_A \boldsymbol{u}) = \nabla \cdot (D \nabla \rho_A), \tag{63}$$

where D denotes the diffusion coefficient of species A in the solution that is supposed to be constant. Under hypotheses 1 and 3, the jump condition across interface Σ gives the relation

$$-\rho_g \dot{R} = \rho_A (u - \dot{R}) - D \frac{\partial \rho_A}{\partial r} \quad \text{at} \quad \big(R(t), t\big). \tag{64}$$

Applying the boundary condition on velocity (Eq. 61) along with hypothesis 5, we obtain

$$(\rho_g - \omega \rho^*_{A,l}) \dot{R}(t) = D \frac{\partial \rho_A}{\partial r} \big(R(t), t\big) \quad \text{with} \quad \omega = 1 - \varepsilon. \tag{65}$$

Applying hypothesis 2 and using (Eq. 63) together with the velocity evolution (Eq. 62), the conservation equation for species A satisfies the equation

$$r^{n-1} \frac{\partial \rho_A}{\partial t} + \varepsilon R^{n-1} \dot{R} \frac{\partial \rho_A}{\partial r} = D \frac{\partial}{\partial r} \left(r^{n-1} \frac{\partial \rho_A}{\partial r} \right), \tag{66}$$

where the entire equation has been multiplied by r^{n-1}. This equation is subjected to the following initial and boundary conditions:

$$\forall r > 0, \quad \rho_A(r, 0) = \rho^\infty_{A,l} \qquad \text{initial condition,} \tag{67a}$$

$$\forall t > 0, \quad \rho_A\big(R(t), t\big) = \rho^*_{A,l} \qquad \text{boundary condition at } \Sigma \text{ (hyp. 5),} \tag{67b}$$

$$\forall t > 0, \quad \rho_A(\infty, t) = \rho^\infty_{A,l} \qquad \text{boundary condition at infinity (hyp. 6).} \tag{67c}$$

Let us seek solutions to (Eq. 66) subject to the initial and boundary conditions (Eq. 67a), (Eq. 67b), and (Eq. 67c) together with the jump condition (Eq. 65). There exists a functional relationship φ that relates $\rho_A(r, t)$ to the other variables, satisfying

$$\rho_A(r, t) - \rho^\infty_{A,l} = \varphi(\rho^*_{A,l} - \rho^\infty_{A,l}, \rho_g - \omega \rho^*_{A,l}, D, \varepsilon, r, t).$$

According to the Vaschy-Buckingham theorem, using $\rho^*_{A,l} - \rho^\infty_{A,l}$, D, and t as fundamental units, this relation can be rewritten as

$$\frac{\rho_A(r,t)-\rho^{\infty}_{A,l}}{\rho^{*}_{A,l}-\rho^{\infty}_{A,l}} = \varphi\left(\frac{r}{\sqrt{4Dt}},\varepsilon,\tau\right) \quad \text{with} \quad \tau = \frac{\rho_g-\omega\rho^{*}_{A,l}}{\rho^{*}_{A,l}-\rho^{\infty}_{A,l}}, \tag{68}$$

where the factor 4 has been introduced to simplify the final expression. Evaluating this expression at $\big(R(t),t\big)$ and applying the boundary condition (Eq. 67b), we obtain

$$1 = \varphi\left(\frac{R(t)}{\sqrt{4Dt}},\varepsilon,\tau\right).$$

Since ε and τ are fixed parameters of the problem, considering that the evolution of mass concentration ρ_A is monotonous between $R(t)$ and infinity, there exists a value $\kappa_{\varepsilon,\tau}$ such that $1 = \varphi\left(\kappa_{\varepsilon,\tau},\varepsilon,\tau\right)$ which leads to the equality

$$\kappa_{\varepsilon,\tau} = \frac{R(t)}{\sqrt{4Dt}}, \quad \text{that is} \quad R(t) = \kappa_{\varepsilon,\tau}\sqrt{4Dt}. \tag{69}$$

Next, we aim to determine the value of the constant $\kappa_{\varepsilon,\tau}$. To achieve this, it is necessary to solve (Eq. 66) by seeking a solution of the form (Eq. 68). To simplify the notation, we introduce the following quantities:

$$\varphi_{\varepsilon,\tau}(\eta) = \varphi\left(\frac{r}{\sqrt{4Dt}},\varepsilon,\tau\right) \quad \text{with} \quad \eta = \frac{1}{2}\frac{r}{\sqrt{Dt}}. \tag{70}$$

The partial derivatives of η with respect to t and r are given by $\frac{\partial\eta}{\partial r} = \frac{1}{\sqrt{4Dt}}$ and $\frac{\partial\eta}{\partial t} = -\frac{\eta}{2t}$, thus, the partial derivatives of ρ_A can be expressed as functions of $\varphi_{\varepsilon,\tau}$

$$\frac{\partial\rho_A}{\partial t} = -(\rho^{*}_{A,l}-\rho^{\infty}_{A,l})\frac{\eta}{2t}\varphi'_{\varepsilon,\tau}(\eta), \tag{71a}$$

$$\frac{\partial\rho_A}{\partial r} = \frac{\rho^{*}_{A,l}-\rho^{\infty}_{A,l}}{\sqrt{4Dt}}\varphi'_{\varepsilon,\tau}(\eta), \tag{71b}$$

$$\text{and} \quad \frac{\partial^2\rho_A}{\partial r^2} = \frac{\rho^{*}_{A,l}-\rho^{\infty}_{A,l}}{4Dt}\varphi''_{\varepsilon,\tau}(\eta), \tag{71c}$$

where the prime notation denotes the derivative with respect to η. Using (Eq. 71b) and (Eq. 71c), the diffusion term in (Eq. 66) can be expressed as

$$\frac{\partial}{\partial r}\left(r^{n-1}\frac{\partial\rho_A}{\partial r}\right) = \frac{\rho^{*}_{A,l}-\rho^{\infty}_{A,l}}{4Dt}r^{n-1}\left(\frac{n-1}{\eta}\varphi'_{\varepsilon,\tau}(\eta)+\varphi''_{\varepsilon,\tau}(\eta)\right). \tag{72}$$

Using Eq. 69, we can rewrite the $R^{n-1}(t)\dot{R}(t)$ factor as

$$R^{n-1}(t)\dot{R}(t) = 2D(4Dt)^{\frac{n-2}{2}}\kappa_{\varepsilon,\tau}^{n}. \tag{73}$$

Substituting expressions (Eq. 71a), (Eq. 71b), (Eq. 73), and (Eq. 72) into (Eq. 66) and multiplying by $\frac{2t}{r^{n-1}(\rho_{A,l}^{*}-\rho_{A,l}^{\infty})}$, we obtain

$$-\eta\varphi_{\varepsilon,\tau}'(\eta) + \varepsilon\kappa_{\varepsilon,\tau}^{n}\underbrace{\frac{4Dt}{r^{n-1}}(4Dt)^{\frac{n-2}{2}}\frac{1}{\sqrt{4Dt}}}_{\frac{1}{\eta^{n-1}}}\varphi_{\varepsilon,\tau}'(\eta) = \frac{1}{2}\left(\frac{n-1}{\eta}\varphi_{\varepsilon,\tau}'(\eta) + \varphi_{\varepsilon,\tau}''(\eta)\right). \tag{74}$$

Rearranging the terms, we obtain the following ordinary differential equation:

$$\varphi_{\varepsilon,\tau}''(\eta) + \left(\frac{n-1}{\eta} - \frac{2\varepsilon\kappa_{\varepsilon,\tau}^{n}}{\eta^{n-1}} + 2\eta\right)\varphi_{\varepsilon,\tau}'(\eta) = 0. \tag{75}$$

The initial and boundary conditions (Eq. 67a), (Eq. 67b), and (Eq. 67c) yield the constraints:

$$\varphi_{\varepsilon,\tau}(\infty) = 0, \tag{76a}$$

$$\varphi_{\varepsilon,\tau}(\kappa_{\varepsilon,\tau}) = 1, \tag{76b}$$

$$\text{and} \quad \varphi_{\varepsilon,\tau}(\infty) = 0. \tag{76c}$$

Integrating (Eq. 75) once, we obtain, up to a multiplicative constant C,

$$\varphi_{\varepsilon,\tau}'(\eta) = CF(\eta) \quad \text{with} \quad F(\eta) = \begin{cases} \exp(2\varepsilon\kappa_{\varepsilon,\tau}\eta - \eta^2) & \text{if } n = 1, \\ \eta^{-1}\exp\big(2\varepsilon\kappa_{\varepsilon,\tau}^{2}\ln(\eta) - \eta^2\big) & \text{if } n = 2, \\ \eta^{-2}\exp\big(-2\varepsilon\kappa_{\varepsilon,\tau}^{2}\eta^{-1} - \eta^2\big) & \text{if } n = 3. \end{cases} \tag{77}$$

To determine the constant C, we use the mass concentration jump condition (Eq. 65) along with (Eq. 71b):

$$(\rho_g - \omega\rho_{A,l}^{*})\frac{2D\kappa_{\varepsilon,\tau}}{\sqrt{4Dt}} = D\frac{\rho_{A,l}^{*} - \rho_{A,l}^{\infty}}{\sqrt{4Dt}}\varphi_{\varepsilon,\tau}'(\kappa_{\varepsilon,\tau}). \tag{78}$$

Substituting $\varphi_{\varepsilon,\tau}'(\kappa_{\varepsilon,\tau})$ with $CF(\kappa_{\varepsilon,\tau})$ and rearranging the terms gives

$$CF(\kappa_{\varepsilon,\tau}) = 2\tau\kappa_{\varepsilon,\tau}. \tag{79}$$

Thus, the solution is given by

$$\varphi'_{\varepsilon,\tau}(\eta) = 2\tau\kappa_{\varepsilon,\tau}\frac{F(\eta)}{F(\kappa_{\varepsilon,\tau})}. \tag{80}$$

Integrating (Eq. 80) with respect to η from $\kappa_{\varepsilon,\tau}$ to infinity gives

$$\varphi_{\varepsilon,\tau}(\infty) - \varphi_{\varepsilon,\tau}(\kappa_{\varepsilon,\tau}) = \frac{2\tau\kappa_{\varepsilon,\tau}}{F(\kappa_{\varepsilon,\tau})}\int_{\kappa_{\varepsilon,\tau}}^{\infty} F(\eta)\,\mathrm{d}\eta. \tag{81}$$

Applying the boundary conditions (Eq. 76b) and (Eq. 76a), the value of the growth coefficient is obtained by solving one of the following equation for $\kappa_{\varepsilon,\tau}$, depending on the dimension n

$$-1 = 2\tau\kappa_{\varepsilon,\tau}\exp(\kappa_{\varepsilon,\tau}^2 - 2\varepsilon\kappa_{\varepsilon,\tau}^2)\int_{\kappa_{\varepsilon,\tau}}^{\infty}\exp(2\varepsilon\kappa_{\varepsilon,\tau}\eta - \eta^2)\,\mathrm{d}\eta \qquad \text{for } n = 1, \tag{82a}$$

$$-1 = 2\tau\kappa_{\varepsilon,\tau}^2\exp\big(\kappa_{\varepsilon,\tau}^2 - 2\varepsilon\kappa_{\varepsilon,\tau}^2\ln(\kappa_{\varepsilon,\tau})\big)\int_{\kappa_{\varepsilon,\tau}}^{\infty}\eta^{-1}\exp\big(2\varepsilon\kappa_{\varepsilon,\tau}^2\ln(\eta) - \eta^2\big)\,\mathrm{d}\eta \qquad \text{for } n = 2, \tag{82b}$$

$$-1 = 2\tau\kappa_{\varepsilon,\tau}^3\exp\big(\kappa_{\varepsilon,\tau}^2 + 2\varepsilon\kappa_{\varepsilon,\tau}^2\big)\int_{\kappa_{\varepsilon,\tau}}^{\infty}\eta^{-2}\exp\big(-2\varepsilon\kappa_{\varepsilon,\tau}^3\eta^{-1} - \eta^2\big)\,\mathrm{d}\eta \qquad \text{for } n = 3, \tag{82c}$$

where τ defined in (Eq. 68) can be rewritten as $\tau = \frac{\rho_g}{\rho_l}\frac{\rho_l - \rho_{A,l}^*}{\rho_{A,l}^* - \rho_{A,l}^\infty}$.